https://doi.org/10.5194/wes-2025-69
Preprint. Discussion started: 6 May 2025

Modelling vortex generators effects on turbulent boundary layers with integral boundary layer equations

Abhratej Sahoo[1,2], Akshay Koodly Ravishankara[1], Wei Yu[2], Daniele Ragni[2], and Carlos Simao Ferreira[2]
[1]TNO Wind Energy
[2]TU Delft Aerospace Engineering
Correspondence: Abhratej Sahoo (A.Sahoo@tudelft.nl)

Abstract. Vortex generators (VGs) are known to delay separation and stall, allowing the design of airfoils with larger stall margins, particularly for thick airfoil sections in the in-board and mid-board regions of modern slender wind turbine blades. Including VG effects in blade design studies requires accurate VG models for fast lower-order techniques, like Integral Boundary Layer (IBL) methods. Previous VG models for IBL methods use engineering approaches tuned on airfoil aerodynamic data. The accuracy of these models depends on the availability of wind tunnel aerodynamic polar datasets for tuning, which are limited and time-consuming to expand for the relevant wind conditions, airfoil sections, and VG configurations being used in continuously growing wind turbine blades. This work proposes a VG model derived from flat plate boundary layers under the influence of VGs. The new VG model empirically models the shape factor of the boundary layer and the viscous dissipation coefficient in the IBL framework to account for the additional momentum and dissipation in the boundary layer mean flow due to VGs. The model is developed from a wide range of flat plate boundary layers and VGs to account for variations in VG vane size and placement on the turbulent boundary layer development influencing the airfoil aerodynamic characteristics. The new VG model is implemented in an in-house code RFOIL, an improvement over XFOIL, validated with CFD data and wind tunnel measurements of flat plates and airfoil sections equipped with VGs. The new VG model RFOILVogue better captures the positive stall characteristics than the existing VG models for IBL equations. Cases with severe adverse pressure gradients are identified as areas of improvement for the developed VG model, and a methodology is proposed for future work.

1 Introduction

Studies on the projected capacity of future wind turbine rotors indicate an increasing trend for larger rotors with lower induction and blades far beyond 100 metres in radius (Jensen et al., 2017; Schepers et al., 2015). Relatively thicker airfoils must be employed along the entire blade span to balance the aero-structural loads, ensure structural integrity, and reduce deformations. These thicker airfoils are more prone to flow separation, with the consequent loss in lift leading to a decrease in annual energy production (AEP) and an increase in fatigue loading, affecting the structural health of the blades (McKenna et al., 2016). Vortex generators (VGs) are conventionally adopted as passive flow control devices, primarily delaying flow separation at moderate angles of attack and consequently improving the maximum lift of these thicker airfoil sections (Lin, 2002; Baldacchino et al., 2018). With turbines growing in size, it is common to see their installation up to the most outboard blade sections to ensure

https://doi.org/10.5194/wes-2025-69
Preprint. Discussion started: 6 May 2025

eawe european academy of wind energy
Open Access WIND ENERGY SCIENCE DISCUSSIONS

optimal aerodynamic performance in a broader range of operating conditions (Bak et al., 2016). Their application has additionally been shown to mitigate the effects of leading-edge erosion, partially restoring the original airfoil design conditions (Gutiérrez et al., 2020; Ravishankara et al., 2020). The performance prediction of VGs becomes very important in the design phase to avoid unacceptable changes in loading, especially considering their installation on progressively outboard sections on the blade.

While wind tunnel campaigns and numerical modelling with Computational Fluid Dynamics (CFD) are sufficient to analyse the effect of VGs on 3D boundary layers and flow separation characteristics as add-ons, high-fidelity computations can actually prove prohibitive in including VGs in blade design optimisation routines due to computational costs (Aparicio et al., 2015; Gonzalez et al., 2016; Gonzalez-Salcedo et al., 2020). Despite the development of partly-modelled and partly-resolved approaches like the Bender–Anderson–Yagle (BAY) model (Bender et al., 1999; Jirásek, 2005; Manolesos et al., 2020) to aid faster CFD analysis of VGs, as well as recent advances in computational capacity, these methods still require a significant computational time of the order of several weeks. Blade design optimisation routines usually employ reduced-order, computationally efficient tools like XFOIL (Drela, 1989) and RFOIL (Van Rooij, 1996) developed using flow field data from higher-order methods like CFD or flow measurements. XFOIL and RFOIL couple an inviscid panel method to a viscous boundary layer solver based on the Integral Boundary Layer (IBL) equations. Both tools excel in predicting the lift and drag characteristics of airfoils in natural and forced transition at low and medium angles of attack just after stall, with limited capabilities for deep stall (Drela, 1989; Van Rooij, 1996).

Previous studies in literature have proposed modelling the effect of the streamwise vortices caused by VGs as an additional source of turbulence in the boundary layer to predict the performance of VGs with IBL equations correctly. Kerho and Kramer (Kerho and Kramer, 2003) proposed modifying the equation of turbulent shear stress lag (Green et al., 1977) in the system of IBL equations by including the added turbulence as a source term. Modification of the turbulent shear stress lag equation was also the fundamental basis of the engineering models developed by De Tavernier et al. (De Tavernier et al., 2018) and Daniele et al. (Daniele et al., 2019). All three previous models employed a source term that appears at the VG location and dissipates downstream of the VG location to incorporate the effect of VGs as extra turbulence production in the boundary layer. All three models used tunable coefficients in the source term formulation for representative test cases. The implementation of De Tavernier et al. adopted a multivariate regression of several coefficients based on the lift polars of a larger database of airfoils and VG parameters, leading to a more widely usable implementation in XFOIL called XFOILVG. XFOILVG's implementation has also been coupled to a double-wake panel method for dynamic stall calculations of airfoils equipped with VGs (Yu et al., 2024).

In the past work of Sahoo et al. (2024), the authors validated the added turbulent source term model and its assumptions. The VG model from De Tavernier et al. (2018) was implemented in RFOIL, an improvement over XFOIL, and the lift behaviour predictions of both RFOILVG and XFOILVG were benchmarked against an extensive database of aerodynamic data of airfoil sections with different VG geometries. The benchmark showed that XFOILVG and RFOILVG over-predicted the maximum positive lift and stall angle for airfoils and VGs outside the training dataset. This was also seen in the work of Yu et al. (2024). The benchmark concluded that the only way of improving such an engineering model is by training it on broader datasets

https://doi.org/10.5194/wes-2025-69
Preprint. Discussion started: 6 May 2025

eawe european academy of wind energy
Open Access WIND ENERGY SCIENCE DISCUSSIONS

representative of the changing VG types, airfoils, and Reynolds numbers for modern wind turbines. The lack of wind tunnel data for relatively thicker airfoils with VGs thus limits the improvement of this tuned engineering model.

Literature also shows that the underlying assumption behind previous models — modelling VGs as additional turbulence production in the boundary layer — is incomplete. Numerical and experimental studies on vortices in turbulent boundary layers show that not only turbulent fluctuations but also mean velocity profiles are modified (Squire, 1965; Von Stillfried et al., 2009; von Stillfried et al., 2011; Velte et al., 2014; Baldacchino et al., 2015; Gutierrez-Amo et al., 2018). The mean flow transport due to the vortices causes a redistribution of momentum and energy, leading to changes in all three components of velocities and spatial gradients. In particular, the spanwise velocities, stresses, and gradients can no longer be neglected when formulating the IBL equations from the Navier-Stokes equations. These studies show that statistical models that model the effect of VGs as turbulent forcing under-predict the shear stress and the pressure gradient evolution. Even though changes in the integral boundary layer quantities have been reported independently in literature by Schubauer and Spangenberg (1960); Gould (1956); Lögdberg et al. (2009), existing models do not relate these changes to changes in the mean flow. This work fills this gap with a VG model in the IBL framework that incorporates the changes in the mean flow due to VGs to predict the boundary layer characteristics.

1.1 Present research

In this work, we first present the new IBL equations for VGs, derived from the mean flow changes, containing additional terms to account for the missing factors. We then present a methodology to model the most significant new and modified terms, relating VG array geometry parameters and the flow Reynolds numbers to the modelled IBL quantities. Thus, unlike the previously proposed tuned models that did not account for any vortex dynamics, the proposed VG model relates the changes in IBL quantities to the dynamics of streamwise vortices embedded inside the turbulent boundary layer. This results in an analytical model independent of airfoil tuning data that captures the evolution of IBL quantities in the span and downstream of VGs. The proposed VG model is valid for counterrotating VG arrays, which are the type of array most commonly used in wind turbines, and shown to be the most effective VG arrangement for flow separation control in previous studies in literature (Gould, 1956; Baldacchino et al., 2018).

The manuscript is organised as follows. Section 2 gives a background on the original IBL equations used in XFOIL/RFOIL. Section 3 details the setup of the CFD simulations used to generate the flat plate boundary layer data with and without VGs used to develop the proposed model. Section 4 describes the new equations due to VGs, the most significant IBL terms, and the model to integrate these changes in RFOIL. The implementation in RFOIL is first verified against CFD data in Section 5 by recreating an approximate flat plate in RFOIL. Subsequently, the new model's performance is benchmarked against reference wind tunnel data (summarised in Appendix C) and compared to the old models. Section 6 discusses the model performance for some selected test cases and Section 7 summarises the performance assessment for the complete reference database. Section 8 concludes the manuscript summarising the main improvements, limitations, and an outlook on future work to improve the new model further.

https://doi.org/10.5194/wes-2025-69
Preprint. Discussion started: 6 May 2025

Wind Energy Science Discussions

2 Integral Boundary Layer equations

XFOIL and RFOIL are viscous-inviscid interaction tools that split the flow around airfoils into an inviscid outer flow solved with a linear-vorticity stream function panel method coupled to an inner viscous boundary layer flow solved with the IBL method (Drela, 1989). RFOIL improves over XFOIL's IBL formulation for airfoil sections near stall experiencing 3D rotational flow on wind turbine blades through additional rotational corrections, thick airfoil drag corrections, and numerical stability corrections (Snel et al., 1993, 1994; Van Rooij, 1996; Ramanujam et al., 2016). For the sake of simplicity, we will discuss the VG model using the original XFOIL equations without RFOIL's additional improvement terms. As such, the VG model can be applied to the IBL framework independent of RFOIL's other improvements. The original IBL equations are presented in Equations (1) to (3). Details of their derivation from the Navier Stokes equations can be found in literature such as Whitfield (1978); White (2006); Özdemir (2020).

$$\frac{d\theta}{dx} = \frac{C_f}{2} - (H+2)\frac{\theta}{U_e}\frac{dU_e}{dx} \tag{1}$$

$$\frac{dH^*}{dx} = \frac{2C_\mathcal{D}}{\theta} - \frac{H^*}{\theta}\frac{C_f}{2} - (1-H)\frac{H^*}{U_e}\frac{dU_e}{dx} \tag{2}$$

$$\frac{\delta}{C_\tau}\frac{dC_\tau}{dx} = K_c\left({C_{\tau_{EQ}}}^{\frac{1}{2}} - {C_\tau}^{\frac{1}{2}}\right) + 2\delta\left(\frac{4}{B\delta^*}\left(\frac{C_f}{2} - \left(\frac{H-1}{AH}\right)^2\right) - \frac{1}{U_e}\frac{dU_e}{dx}\right) \tag{3}$$

where δ is the boundary layer thickness, δ^* is the displacement thickness, θ is the momentum thickness, $H = \frac{\delta^*}{\theta}$ is the shape factor, δ^k is the kinetic energy thickness, $H^* = \frac{\delta^k}{\theta}$ is the kinetic energy shape factor, U_e is the edge velocity, C_f is the skin friction coefficient, $C_\mathcal{D}$ is the dissipation coefficient, C_τ is the shear stress coefficient and $C_{\tau_{EQ}}$ is the equilibrium shear stress coefficient. A and B in Equation (3) are the constants of the $G-\beta$ relationship between the scaled pressure gradient $\beta \equiv \frac{2}{C_f}\frac{\delta^*}{u_e}\frac{dU_e}{dx}$ and the shape parameter $G \equiv \frac{H-1}{H}\frac{1}{\sqrt{C_f/2}}$ of the velocity-defect profile (Clauser, 1954). They control the equilibrium shear stress level in the outer layer of the turbulent boundary layer. For natural transition cases, both XFOIL and RFOIL replace the turbulent shear lag equation (Equation (3)) with an equation checking for transition using the e^N method (Van Ingen, 2008).

The inviscid panel code first computes U_e. The inviscid U_e is used as a first estimate for the final solution. The system of IBL equations is solved for the primary variables θ, δ^*, and C_τ. The edge velocity is then updated based on the calculated boundary layer solution. Empirical closure relations relating the secondary variables C_f, H^*, $C_\mathcal{D}$, $C_{\tau_{EQ}}$, and δ to H and Re_θ are used to close the system of equations. These closure relations are derived from families of velocity profiles like the Swafford velocity profile (Swafford, 1983). The viscous and inviscid solutions are coupled using a simultaneous coupling scheme and the simultaneous system is solved with a Newton-Raphson solver described in Drela et al. (1986).

https://doi.org/10.5194/wes-2025-69
Preprint. Discussion started: 6 May 2025

3 Numerical Setup

The boundary layer data used to develop the VG model is generated using Computational Fluid Dynamics (CFD) simulations of flat plates equipped with VGs. CFD is used because of the ease of obtaining high-resolution data in the boundary layer for a broad range of flow parameters and configurations compared to experiments. The simulations are performed using the open source tool SU2 (Economon et al., 2016), a compressible flow solver with density-based preconditioning and artificial compressibility options for low Mach number incompressible flows (Economon, 2020).

The simulations recreate the experimental setup of Baldacchino et al. (2015). The VG array employed is an array of counter-rotating rectangular vanes of height $h = 5\,mm$ and length $l = 12.5\,mm$. The distance between consecutive pairs is $D = 30\,mm$ and between consecutive vanes in a pair is $d = 12.5\,mm$. The vanes are angled at $\beta = 18°$. The simulation domain and VG geometry are presented in Figure 1. A body-fitted mesh is generated over zero-thickness VGs to ensure a well-resolved boundary layer. The VGs are placed so that the trailing edge of the vane is $x_{VG,TE} = 0.985\,m$ over the simulation domain of a flat plate of length 2.0 m to let the flow develop for 225 VG heights downstream of the VG location. The simulation domain spanned the periodic unit of 1 VG pair with periodic boundary conditions in the span-wise direction.

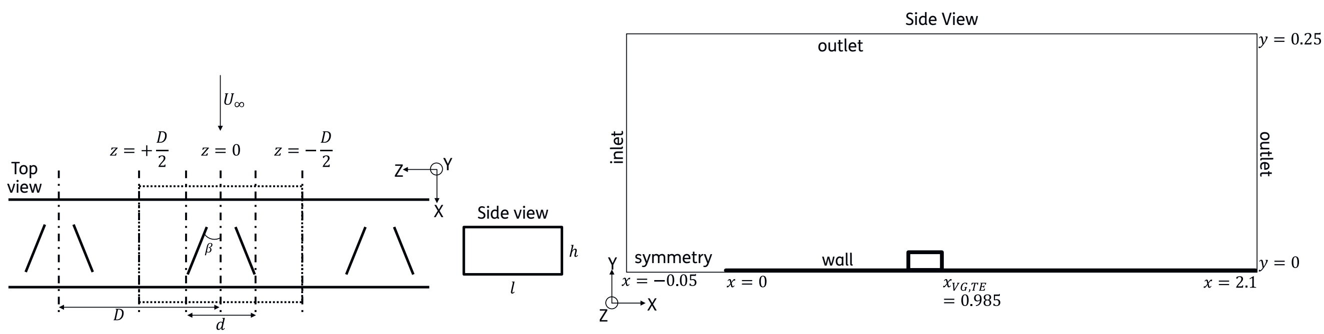

(a) VG Array with simulation domain (in dotted lines)

(b) Boundary conditions (all values in metres)

Figure 1. Sketch of the simulation domain and geometry and imposed boundary conditions.

The steady, incompressible, fully-turbulent Reynolds-averaged Navier-Stokes (RANS) simulations are performed with a Spalart-Almaras (SA) turbulence model (Spalart and Allmaras, 1992) for the no VG and VG setups. The single equation SA turbulence model is chosen for its simplicity and relative insensitivity to grid resolution compared to other models (Bardina et al., 1997). While the SA model can under-predict skin friction for certain flows with lower Re_θ (Spalart and Garbaruk, 2020), it is accurate for the high range of Re_θ investigated in this study. Streamwise Reynolds numbers $Re_x = 1 - 10 \times 10^6\,m^{-1}$ corresponding to an incoming flow with $Re_\theta = 2000 - 14000$ at the VG leading edge location were simulated. The results from $Re_x = 2 \times 10^6\,m^{-1}$ will be used to illustrate the derivation of new IBL equations in this work.

The simulation grid and boundary conditions are adapted for 3D periodic VG simulations from the incompressible turbulent flat plate test case from the SU2 repository (Economon, 2018), which is in turn adapted from the test case described in the NASA turbulence modelling resource (Rumsey et al., 2010). The grid is adapted with additional refinement to better capture

https://doi.org/10.5194/wes-2025-69
Preprint. Discussion started: 6 May 2025

near-VG and near-wall effects. The coarse grid has $415 \times 82 \times 40$ elements in the streamwise (X), wall-normal (Y), and spanwise (Z) directions. The refined grid has $500 \times 300 \times 40$ elements, with mesh refinement near the VG location and in the boundary layer. The mesh refinement in the boundary layer is sketched in Figure 2 and detailed in Table 1. A constant velocity inlet and constant pressure outlets bound the simulation domain. The VGs and the flat plate are prescribed as adiabatic no-slip walls. The surfaces at $z = \pm D/2$ are prescribed with periodic boundary conditions.

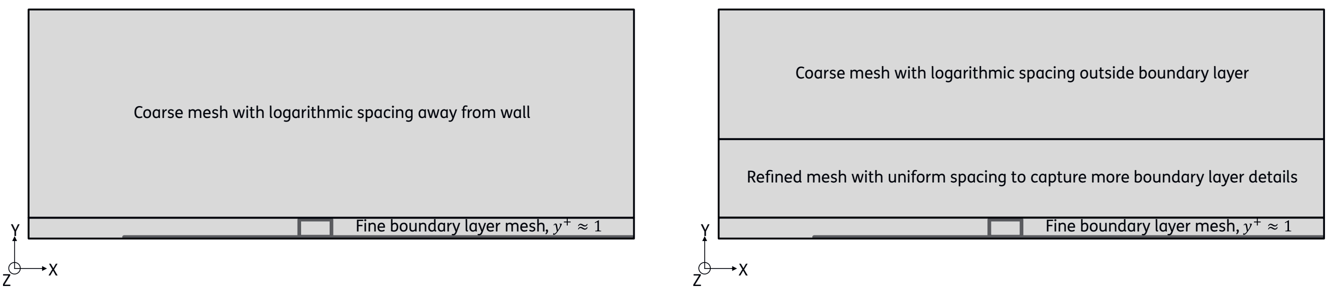

(a) Coarse mesh (around 1.4 million elements)

(b) Fine mesh (around 6 million elements)

Figure 2. Schematic of mesh refinement to better capture the flow details in the boundary layer

Table 1. Comparison of the coarse and refined grids in the Y direction (normal to the wall).

Grid	Region 1	Region 2	Region 3
Coarse Grid	$0 \leq y \leq h_{VG}$ 40 elements, logarithmic spacing $y^+ \approx 1$	$h_{VG} \leq y \leq y_{max}$ 42 elements, logarithmic spacing	—
Refined Grid	$0 \leq y \leq h_{VG}$ 75 elements, logarithmic spacing $y^+ \approx 1$	$h_{VG} \leq y \leq 2.5\delta$ 150 elements, uniform spacing	$2.5\delta \leq y \leq y_{max}$ 75 elements, logarithmic spacing

4 New VG Model

Boundary layer data from the CFD simulations described in Section 3 was used to calculate all the VG and No VG (integral) boundary layer quantities and modelling parameters presented in this section. Since this paper focuses on a VG model derived from the mean flow quantities, the modifications to Equations (1) and (2) form the focus of the paper. Like the original IBL equations, the VG IBL equations can be derived from the boundary layer equations that result from the changes in the mean

https://doi.org/10.5194/wes-2025-69
Preprint. Discussion started: 6 May 2025

eawe european academy of wind energy
Open Access WIND ENERGY SCIENCE DISCUSSIONS

flow of the turbulent boundary layers due to the streamwise vortices produced by the VGs. The modified boundary layer equations and the derivation of the IBL equations from the boundary layer equations are described in Appendix A.

The IBL equations described in subsequent sections are expressed in terms of the spanwise-averaged form of all the IBL quantities, which are henceforth denoted with a '— '. The VG model proposed in this paper is thus limited to predicting the 2D boundary layer characteristics and force coefficients representing the average aerodynamic behaviour in the span.

All spanwise-averaged quantities in this paper are averaged along the span of a repeating VG pair unit in an array of counterrotating VG vanes (sketched in Figure 1a), as described in Equation (4). For those IBL quantities that are defined as ratios of other IBL quantities (e.g. the shape factors H and H^*), the spanwise-averaged form is taken as the spanwise average of the ratio. For example, the spanwise averaged H, a ratio of δ^* to θ, is shown in Equation (5). For the zero pressure gradient flat plate boundary layers, it was verified that both definitions approximately yield the same value, i.e. $\overline{\left(\frac{\delta^*}{\theta}\right)} \approx \frac{\overline{\delta^*}}{\overline{\theta}}$, for example. However, this may not hold for boundary layers with different pressure gradients.

$$\text{For a VG IBL quantity } Q, \quad \overline{Q} = \frac{\int_{-D/2}^{D/2} Q dz}{\int_{-D/2}^{D/2} dz} \tag{4}$$

$$\text{For ratios such as } H, \overline{H} = \overline{\left(\frac{\delta^*}{\theta}\right)} \neq \frac{\overline{\delta^*}}{\overline{\theta}} \tag{5}$$

4.1 Modified IBL equations for VGs

The modified IBL equations for VGs are presented in Equations (6) and (7). The new terms arising from the effect of VGs on the mean flow are highlighted. The IBL momentum equation for counterrotating VGs is identical to the equation without VGs except for the local induced velocity/pressure contribution from the vortices. The increased momentum in the boundary layer appears implicitly through the increased shape factor and the increased skin friction coefficient. The IBL kinetic energy equation (Equation (7)) has two additional terms – the term resulting from the local induced velocity contribution of the vortices and a dissipative term resulting from the spanwise shear stress.

$$\frac{d\overline{\theta}}{dx} = \frac{\overline{C_f}}{2} - \left(\overline{H}+2\right)\frac{\overline{\theta}}{U_e}\frac{dU_e}{dx} + \boxed{\overline{\left(\int_0^\infty \frac{\partial p_{i,VG}}{\partial x} dy\right)}} \tag{6}$$

$$\frac{d\overline{H^*}}{dx} = 2\frac{\overline{C_\mathcal{D}}}{\overline{\theta}} - \frac{\overline{H^*}}{\overline{\theta}}\frac{\overline{C_f}}{2} + \left(\overline{H}-1\right)\frac{\overline{H^*}}{U_e}\frac{dU_e}{dx} + \boxed{\frac{2}{U_e^3\overline{\theta}}\overline{\left(\int_0^\delta \tau_{zx}\frac{\partial u}{\partial z}\right)}} + \boxed{\frac{2}{\rho U_e^3}\overline{\left(\int_0^\delta u\frac{\partial p_{i,VG}}{\partial x} dy\right)}} \tag{7}$$

The new dissipative term has a similar form as the already existing viscous dissipation term $C_\mathcal{D}$ from the no-VG boundary layers, as shown in Equation (8). We denote the VG dissipation term as $C_{\mathcal{D}z}$ to indicate that it arrives from the spanwise stresses. In the final equations, the sum of both dissipation terms is combined into one term $C_{\mathcal{D},total}$.

https://doi.org/10.5194/wes-2025-69
Preprint. Discussion started: 6 May 2025

$$C_{\mathcal{D}} = \frac{1}{\rho U_e^3}\int_0^\delta \left(\tau_{yx}\frac{\partial u}{\partial y}\right)dy, \quad \text{and} \quad C_{\mathcal{D}z} = \frac{1}{\rho U_e^3}\int_0^\delta \left(\tau_{zx}\frac{\partial u}{\partial z}\right)dy \tag{8}$$

Taking $\overline{C_{\mathcal{D},total}} = \overline{C_{\mathcal{D}}} + \overline{C_{\mathcal{D}z}}$, the final IBL equations for incompressible turbulent span-averaged boundary layers due to counter-rotating VGs with a common downwash are presented in Equations (9) and (10).

$$\frac{d\overline{\theta}}{dx} = \frac{\overline{C_f}}{2} - \left(\overline{H}+2\right)\frac{\overline{\theta}}{U_e}\frac{dU_e}{dx} + \overline{\left(\int_0^\infty \frac{\partial p_{i,VG}}{\partial x}dy\right)} \tag{9}$$

$$\frac{d\overline{H^*}}{dx} = 2\frac{\overline{C_{\mathcal{D},total}}}{\overline{\theta}} - \frac{\overline{H^*}}{\overline{\theta}}\frac{\overline{C_f}}{2} + \left(\overline{H}-1\right)\frac{\overline{H^*}}{U_e}\frac{dU_e}{dx} + \frac{2}{\rho U_e^3}\overline{\left(\int_0^\delta u\frac{\partial p_{i,VG}}{\partial x}dy\right)} \tag{10}$$

The most significant changes in the new IBL equations for VGs are the modified shape factor $\overline{H}$ and the additional viscous dissipation $\overline{C_{\mathcal{D}z}}$, shown in Figure 4. The rest of the spanwise-averaged IBL quantities $\overline{C_f}$, $\overline{H^*}$, and $\overline{C_{\mathcal{D}}}$ can be calculated accurately through closure equations using $\overline{H}$ and $\overline{Re_\theta}$. The original closure equations are still valid for the VG case and shown in Appendix B for completeness. While the induced pressure terms are significant near the VG, they quickly disappear within 10-15 heights downstream of the VG location (Figure 3). Meanwhile, the significant VG-induced changes in the spanwise-averaged shape factor and dissipation coefficient can persist as far as 150-200 heights downstream of the VG location, as seen in Figure 4. Moreover, the induced pressure terms can depend significantly on the boundary layer state, strength of the pressure gradient, separation, and so on, making it complex to model in a simple VG model with minimal parameters derived from flat plate vortex dynamics. Thus, we focus on the shape factor and viscous dissipation in this paper's proposed VG model. In Section 4.2, we propose an analytical function dependent on the VG array geometry and Reynolds number to obtain the VG shape factor from the no-VG value. In Section 4.3, we model the total viscous dissipation as the sum of the dissipation obtained from the no VG closure relation and a function dependent on the VG array geometry and Reynolds number to obtain the additional VG dissipation.

4.2 Modelling of the Shape Factor

The distribution of the shape factor in the span of one counterrotating VG pair is shown for a few downstream locations in Figure 5. The global minima of the distribution remains constant in the span at the centre line $z = 0$ between the two VG vanes. The peak locations move towards the symmetry lines $z = \pm D/2$ as the vortices drift away from each other, directed by the vane placement and alignment.

We can model this spanwise distribution by using the sum of two symmetric Gaussian distributions equidistant from the centreline $z = 0$ between the two VG vanes. At any given streamwise location x, the expression for a Gaussian distribution as a function of the spanwise coordinate z is given by Equation (11), where the centre $\mu(x)$ and the spread $\sigma(x)$ are assumed to

https://doi.org/10.5194/wes-2025-69
Preprint. Discussion started: 6 May 2025

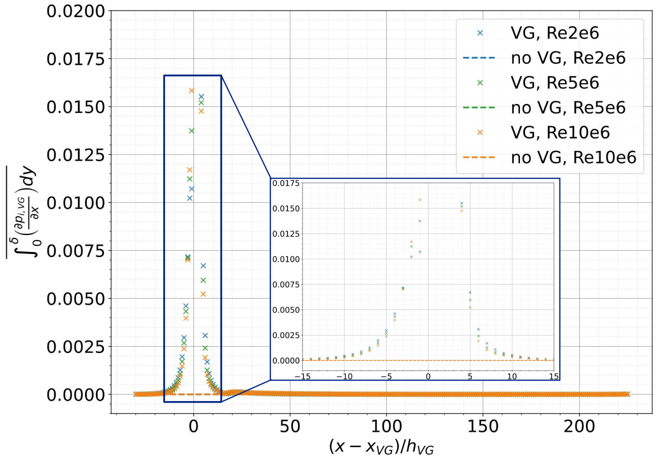

(a) Induced pressure term in the momentum equation

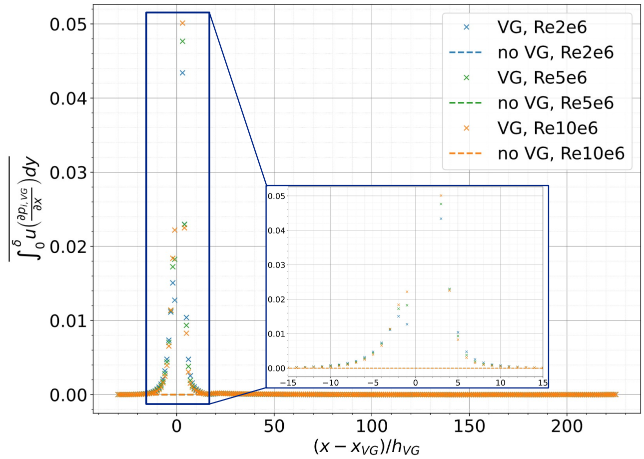

(b) Induced pressure term in the kinetic energy equation

Figure 3. The induced pressure terms are of a significant order of magnitude only in the near field of the VGs

vary only in x. To obtain two Gaussian distributions symmetric about $z = 0$, we can substitute the centre as $\pm\mu(x)$ and get a function $\varphi(x,z)$ as shown in Equation (12). This function can be spanwise averaged with the limits $z = \pm D/2$ to obtain the spanwise-averaged function $\overline{\varphi(x)}$ as shown in Equation (13), where erf denotes the error function.

$$f(x,z) = \frac{1}{\sqrt{2\pi(\sigma(x))^2}} \exp\left(-\frac{(z-\mu(x))^2}{2(\sigma(x))^2}\right) = \frac{1}{\sigma(x)\sqrt{2\pi}} \exp\left(-\frac{1}{2}\left(\frac{z-\mu(x)}{\sigma(x)}\right)^2\right) \tag{11}$$

$$\varphi(x,z) = \frac{1}{\sigma(x)\sqrt{2\pi}} \left(\exp\left(-\frac{1}{2}\left(\frac{z-\mu(x)}{\sigma(x)}\right)^2\right) + \exp\left(-\frac{1}{2}\left(\frac{z+\mu(x)}{\sigma(x)}\right)^2\right)\right) \tag{12}$$

$$\overline{\varphi(x)} = \frac{\int_{-D/2}^{D/2} \varphi(x,z)\,dz}{\int_{-D/2}^{D/2} dz} = \mathrm{erf}\left(\frac{0.5-\mu(x)}{\sigma(x)\sqrt{2}}\right) + \mathrm{erf}\left(\frac{0.5+\mu(x)}{\sigma(x)\sqrt{2}}\right) \tag{13}$$

To model the VG shape factor, we multiply the corresponding no-VG value with this transformation function $\overline{\varphi(x)}$ as shown in Equations (14) and (15). An instance of using this transformation function on the flat plate CFD data is shown in Figure 6a at a streamwise location 10 heights downstream of the VG location. This approximation slightly deviates from the actual shape in the span but accurately estimates the spanwise-averaged shape factor, as seen in Figure 6b. Thus, the VG model in this work predicts the spanwise-averaged values of IBL quantities and cannot predict the accurate variation of IBL quantities in the span.

$$H_{VG}(x,z) = H_{noVG}\varphi(x,z) \tag{14}$$

https://doi.org/10.5194/wes-2025-69
Preprint. Discussion started: 6 May 2025

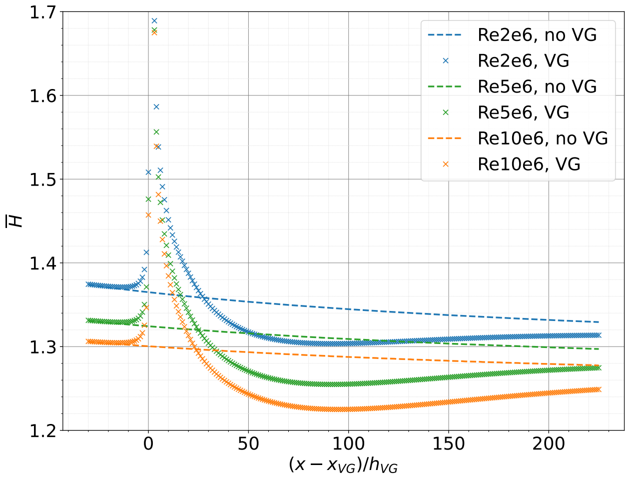

(a) Shape Factor

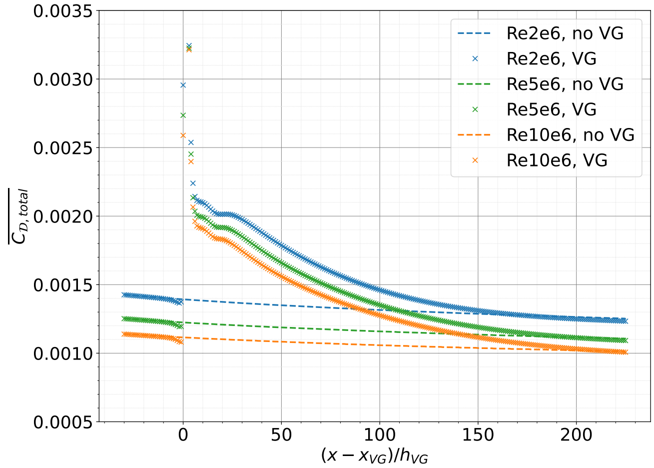

(b) Total viscous dissipation coefficient

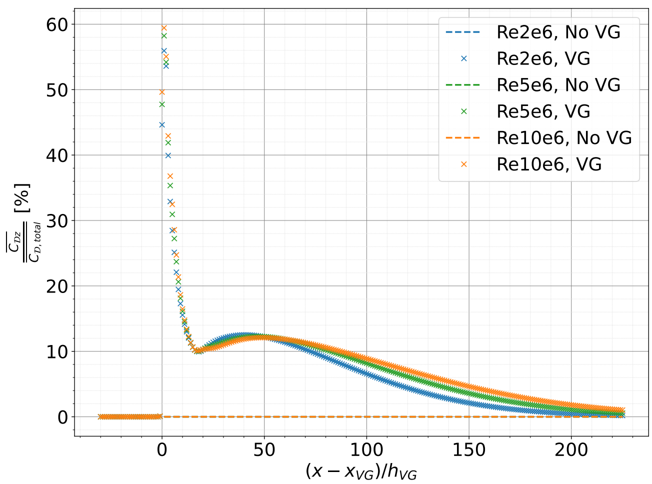

(c) Contribution of the spanwise viscous dissipation to the total dissipation

Figure 4. Comparison of the VG and no VG shape factor and viscous dissipation coefficient for the flat plate with VGs case described in Section 3. The spanwise viscous dissipation contribution persists for 180 heights downstream of the VG location, while changes in the shape factor can persist more than 200 heights downstream of the VGs

$$\overline{H_{VG}(x)} = H_{noVG}\overline{\varphi(x)} \tag{15}$$

To obtain this model in non-dimensional form, the streamwise coordinate x is converted to the relative distance to the VG location and scaled with the VG vane height as $\tilde{x} = (x - x_{VG})/h_{VG}$. The centre of the Gaussian distributions $\mu(\tilde{x})$ is taken

https://doi.org/10.5194/wes-2025-69
Preprint. Discussion started: 6 May 2025

Wind Energy Science Discussions

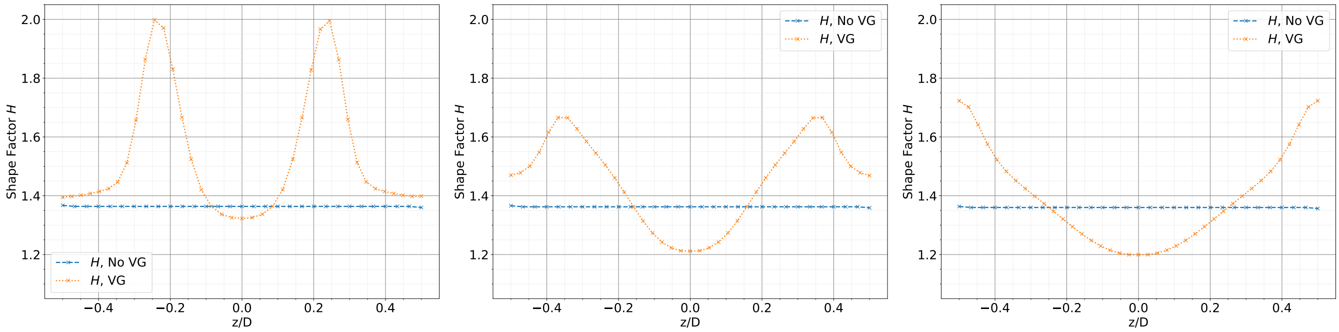

(a) $(x - x_{VG})/h_{VG} = 5.0$ (b) $(x - x_{VG})/h_{VG} = 10.0$ (c) $(x - x_{VG})/h_{VG} = 20.0$

Figure 5. Distribution of the shape factor in the span shown for 5, 10, and 20 heights downstream of the VG location for a flat plate equipped with VGs of 5 mm height.

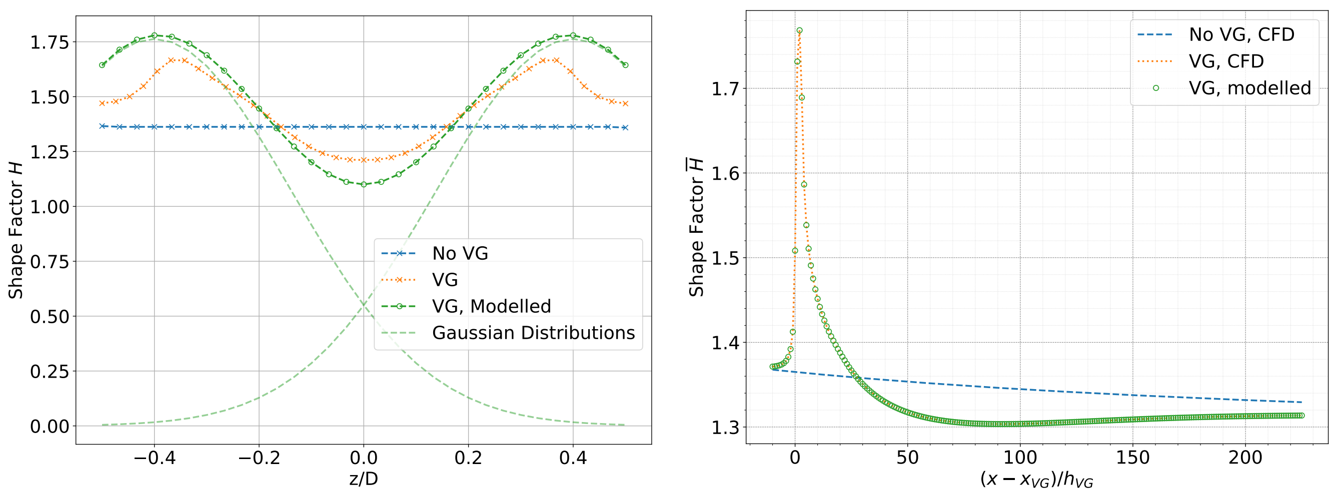

(a) Spanwise distribution at streamwise location $\frac{x-x_{VG}}{h_{VG}} = 10.0$ (b) Spanwise-Averaged

Figure 6. Comparison of actual shape factor to the approximation as the sum of two Gaussian distributions for a flat plate equipped with VGs of 5 mm height at 2 million Reynolds number. The approximation produces an accurate spanwise-averaged value but with some inaccuracies in the span.

to follow a path downstream of the VG location directed by the orientation and placement of the VG vanes, as sketched in Figure 7. The spread parameter of the Gaussian distributions $\sigma(\tilde{x})$ is a function of the local Reynolds number Re_θ as shown in Figure 8. Both $\mu(\tilde{x})$ and $\sigma(\tilde{x})$ are also scaled with the spacing between VG pairs D to generalise the expressions for different VG array spacings.

https://doi.org/10.5194/wes-2025-69
Preprint. Discussion started: 6 May 2025

eawe european academy of wind energy
Open Access WIND ENERGY SCIENCE DISCUSSIONS

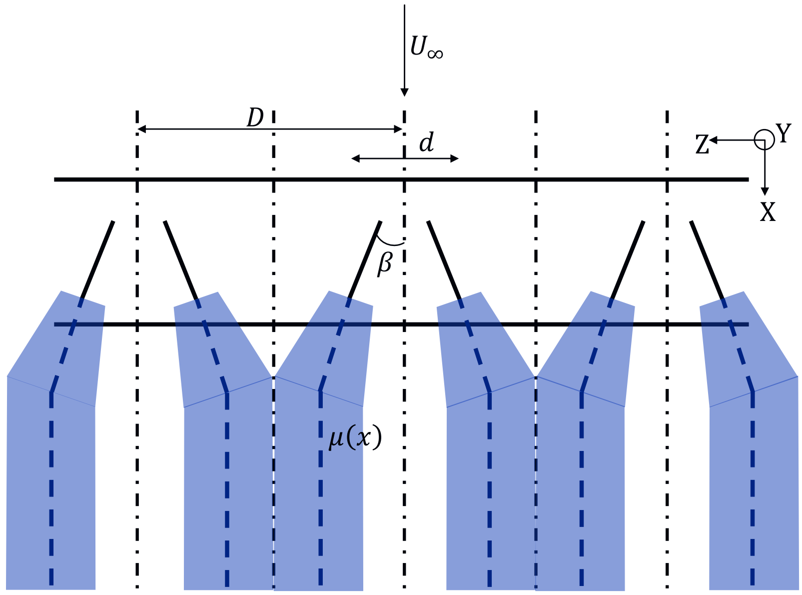

Figure 7. Visualising the distribution of the shape factor as the sum of Gaussian distributions in the XZ plane. The centre of the distributions $\mu(\tilde{x})$ is sketched with blue dashed lines.

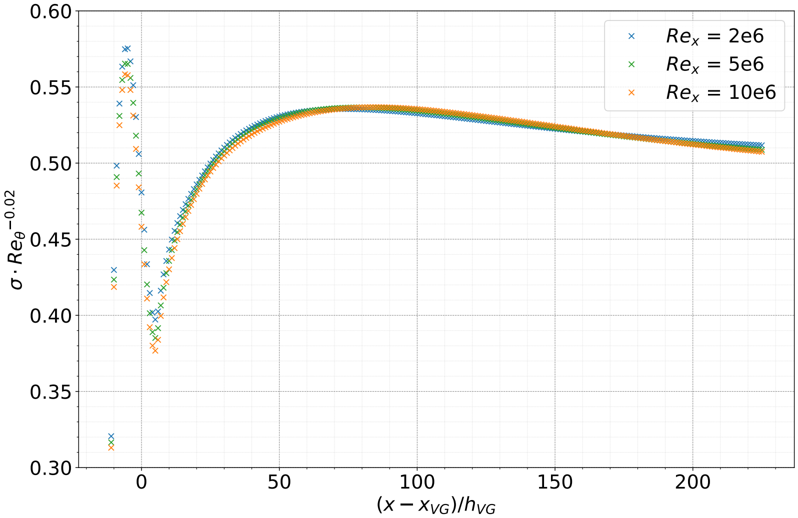

Figure 8. The spread parameter $\sigma(\tilde{x})$ of the shape factor model is a function of Reynolds number and the relative distance to the VG location scaled with the vane height.

https://doi.org/10.5194/wes-2025-69
Preprint. Discussion started: 6 May 2025

4.3 Modelling of the Viscous Dissipation Coefficient

The total dissipation coefficient $\overline{C_{\mathcal{D},total}} = \overline{C_{\mathcal{D}}} + \overline{C_{\mathcal{D}z}}$ consists of the existing $\overline{C_{\mathcal{D}}}$ and the additional VG contribution $\overline{C_{\mathcal{D}z}}$. While verifying the closure equations in Appendix B, it was verified that $\overline{C_{\mathcal{D}}}$ can be calculated with the pre-existing no-VG closure equation if the correct shape factor and Reynolds number are used. Thus, only the new VG contribution $\overline{C_{\mathcal{D}z}}$ needs to be modelled. Just like the σ parameter for the shape factor in Section 4.2, $\overline{C_{\mathcal{D}z}}$ can also be expressed as a function of the VG height-scaled relative downstream location $\tilde{x}$ and $\overline{Re_\theta}$ as shown in Figure 9. Thus, the total viscous dissipation is modelled as described in Equation (16), where the shape factor $\overline{H}$ is modelled as described in Section 4.2.

$$\overline{C_{\mathcal{D},total}}\left(\tilde{x}, Re\right) = \overline{C_{\mathcal{D}closure}}\left(\overline{H}, Re\right) + \overline{C_{\mathcal{D}z}}\left(\tilde{x}, Re\right), \quad \text{where} \quad \tilde{x} = \frac{x - x_{VG}}{h_{VG}} \tag{16}$$

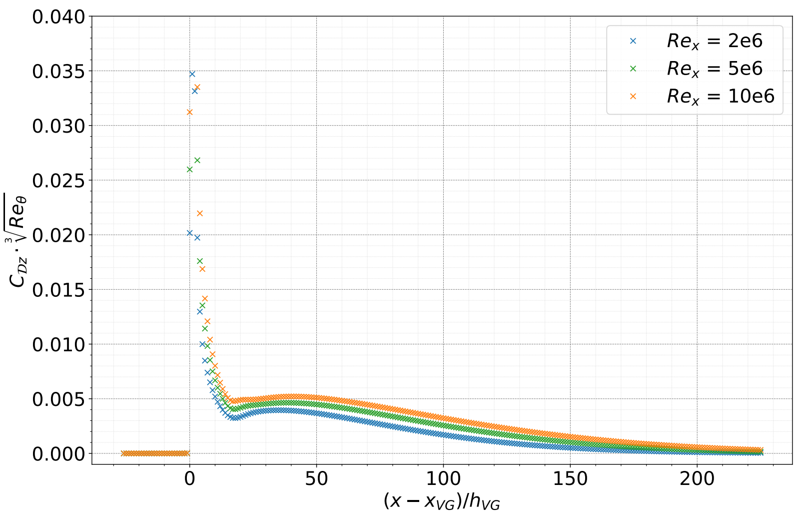

Figure 9. Additional viscous dissipation due to VGs $C_{\mathcal{D}z}$ is a function of Reynolds number and the relative distance to the VG location scaled with the vane height

4.4 Modelling transition to turbulence and upstream effects

The previous VG models for IBL solvers (De Tavernier et al., 2018; Daniele et al., 2019) have assumed that the transition to turbulent flow occurs at the VG location if the incoming boundary layer is laminar. Consequently, the inclusion of the effect of VGs on the boundary layer also started at the VG location. The comparison of the VG and no VG IBL quantities shows an upstream impact of the VGs, particularly on the shape factor in Figure 4a. To include the upstream effects, the proposed model assumes that the transition to a turbulent boundary occurs upstream of the actual VG location. The shape factor and viscous dissipation in Figure 4, the VG values start deviating from the clean values 10 heights upstream of the VG location. Thus, the effects are triggered 10 vane heights upstream of the VG location, as described in Equation (17).

https://doi.org/10.5194/wes-2025-69
Preprint. Discussion started: 6 May 2025

$$x_{tr} = \begin{cases} x_{VG} - 10h_{VG}, & \text{if } x_{tr} > (x_{VG} - 10h_{VG}) \\ x_{tr}, & \text{otherwise} \end{cases} \tag{17}$$

5 Verification of the new model

The VG model implementation in RFOIL was verified by recreating the turbulent flat plate CFD setup in RFOIL. The NASA SC(2)-0402 airfoil (Harris, 1990) with a maximum thickness-to-chord ratio of 2% was chosen for this verification exercise. The aerodynamic properties of the airfoil were calculated in RFOIL at an angle of attack of 1° for a chord-wise Reynolds number of 2 million with transition to turbulence forced at 5% chordwise location on both sides of the airfoil. This gave an approximately zero pressure gradient on the upper surface downstream of the chordwise location $x/c = 0.15$ (as seen in Figure 10a) and a boundary layer development that closely approximates the one seen on the turbulent flat plate in the CFD simulations(Figure 10b). The VG case is recreated by placing a VG array of rectangular vanes at a chordwise location of $x/c = 0.15$ with the same array geometry parameters modelled in the CFD simulations.

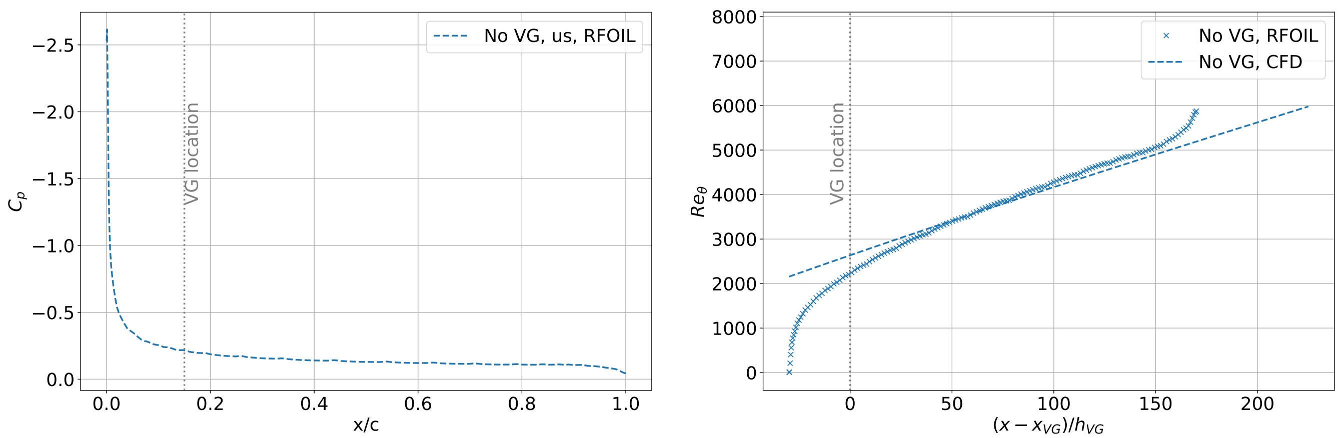

(a) Zero Pressure Gradient on the upper side of the airfoil

(b) Boundary layer growth on the airfoil mimics the flat plate

Figure 10. Recreating the flat plate zero pressure gradient turbulent boundary layer from CFD simulations in RFOIL with the NASA SC(2)-0402 airfoil at 1° angle of attack.

The integral boundary layer properties calculated by RFOIL using the VG model are shown in Figure 11. The RFOIL VG model calculations predict a higher mixing due to VGs than the simulations. This is seen in the model's accurate prediction for the momentum thickness θ but under-prediction for the displacement thickness δ^* in the nearfield of the VGs. However, the overall trend is captured well. The VGs produce a larger relative increase of the momentum thickness than the displacement thickness, resulting in a lower shape factor downstream of the VGs. A lower shape factor than expected means that the model overestimates the mixing produced by VGs compared to CFD calculations. This is also reflected in the secondary IBL param-

https://doi.org/10.5194/wes-2025-69
Preprint. Discussion started: 6 May 2025

eters like skin friction and total viscous dissipation. A lower shape factor estimation results in higher skin friction and viscous dissipation estimates.

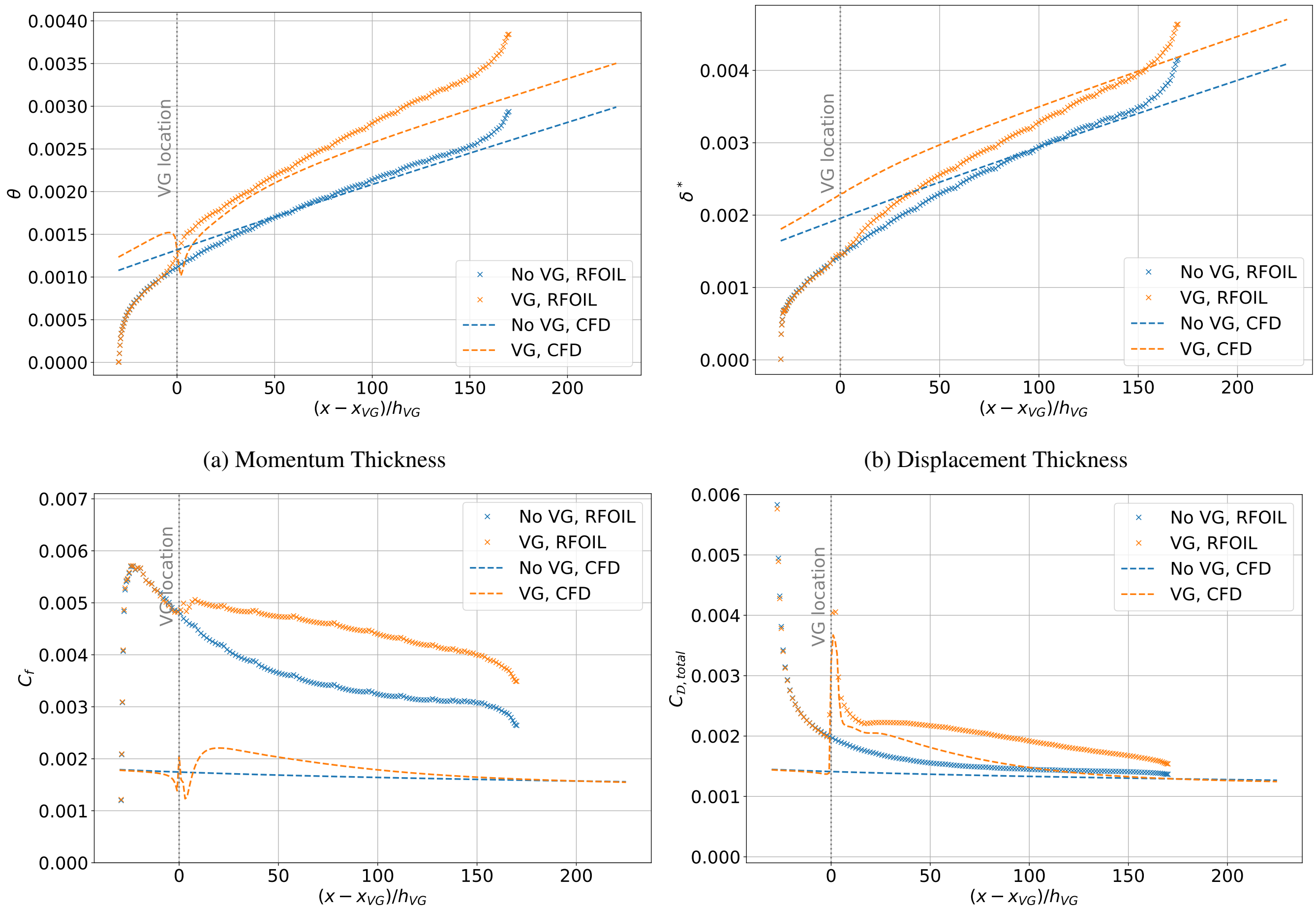

(c) Skin friction coefficient

(d) Total viscous dissipation coefficient

Figure 11. Verifying the VG model implementation in RFOIL by comparing the IBL quantities from the flat plate CFD calculations with an approximated turbulent flat plate in RFOIL.

6 Validation of VG Model

The proposed VG model is validated against wind tunnel lift polar for airfoils, focusing on the changes in positive stall angle and maximum lift between the no VG and VG conditions. The validation database, summarised in Appendix C, consists of thicker airfoils (greater than 21% thickness to chord ratio) tested at chord-wise Reynolds numbers above 1 million, with and without VGs, in natural and forced transition conditions. In all comparisons, the new VG model is also compared to the current

WIND ENERGY SCIENCE DISCUSSIONS

state-of-the-art models of XFOILVG and RFOILVG. The present VG model is denoted as "RFOILVogue" in all subsequent comparisons.

The experimental database used in the benchmark is split into two categories — data used to tune XFOILVG and RFOILVG, and data outside the tuning dataset. The VG model implemented in XFOILVG and RFOILVG uses the lift polars of the airfoils and VGs in the tuning dataset to correct the lift slope of the no-VG polar to the target VG polar. Thus, the subsequent benchmark is presented in two parts. Section 6.1 is the evaluation of RFOILVogue's performance for an FFA-W3-241 airfoil with VGs. This airfoil was not used to develop XFOILVG/RFOILVG's tuned VG model. Thus, it highlights the accuracy and robustness improvements offered by RFOILVogue's analytical VG model for any general airfoil and VG configuration. We also discuss RFOILVogue's performance for a DU-97-W-300 airfoil, which is from XFOILVG/RFOILVG's tuning dataset in Section 6.2 to compare the analytical VG model to the engineering tuning approach.

6.1 Comparison for the FFA-W3-241 airfoil

The first benchmark case chosen for comparison is the flow over an FFA-W3-241 airfoil with a maximum thickness-to-chord ratio of 24.1%. The airfoil features in the new IEA Wind 22 MW Offshore Reference Turbine (Zahle et al., 2024) and is thus considered representative of a typical modern wind turbine rotor blade section. Moreover, this airfoil was not used to tune the VG model implemented in XFOILVG and RFOILVG, which makes it a perfect test case to compare the effectiveness of the older tuned VG models to the improvements produced by the proposed model. The wind tunnel data (Fuglsang et al., 1998) comes from the tests performed by RISO in the VELUX wind tunnel in Denmark. The model chord is $0.6\,m$, and the chord-wise Reynolds number is 1.6 million. The tests are performed in free and forced transition to simulate leading edge erosion effects, as well as with and without VGs. Transition to turbulence is forced using a zigzag trip tape of $0.35\,mm$ thickness. The trip tape was mounted at $x/c = 0.05$ on the suction side and $x/c = 0.10$ on the pressure side. The reported turbulence level corresponded to $N = 2.622$ for the e^N transition check for the free transition calculations.

First, the performance of base RFOIL and XFOIL without VGs is compared to the wind tunnel data. It can be seen in Figure 12 that RFOIL over-predicts the positive stall angle of attack by about $1°$ for the free transition case and about $2°$ for the forced transition case. The slope of the lift polar in RFOIL is also higher, resulting in an over-prediction of the maximum positive lift.

The VG cases consist of triangular vane VGs placed in a counterrotating array on the upper side of the airfoil with the following geometry parameters:

- $h = 4\,mm$, $l = 12\,mm$, $D = 28\,mm$, $d = 20\,mm$, $\beta = 19.5°$, denoted henceforth as the '4 mm VGs'
- $h = 6\,mm$, $l = 18\,mm$, $D = 35\,mm$, $d = 25\,mm$, $\beta = 19.5°$, denoted henceforth as the '6 mm VGs'

When comparing the results for the VG cases in Figures 13 and 14, the higher lift polar slope compared to wind tunnel measurements can be seen for both the previous VG models (XFOILVG and RFOILVG) and the current VG model (RFOILVogue). RFOILVG and RFOILVogue predict the same lift polar slope in the linear region. However, RFOILVogue better captures the stall onset for both the stall angle of attack and the maximum lift. The improvements are higher for the 4 mm VGs than the

https://doi.org/10.5194/wes-2025-69
Preprint. Discussion started: 6 May 2025

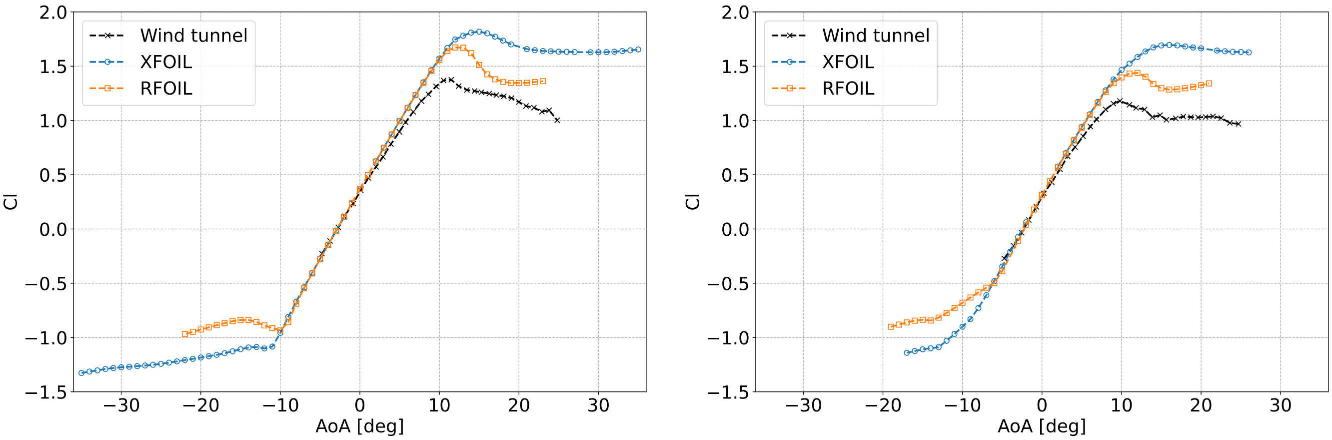

(a) Free transition

(b) Forced transition

Figure 12. Establishing a baseline for RFOIL and XFOIL by comparing the lift characteristics of the FFA-W3-241 airfoil without VGs at 1.6 million Reynolds number with and without forced transition. Wind tunnel data taken from Fuglsang et al. (1998).

6 mm VGs, with about 26% improvement in capturing the maximum lift at stall for the 4 mm VGs compared to about 15% improvement for the 6 mm VGs.

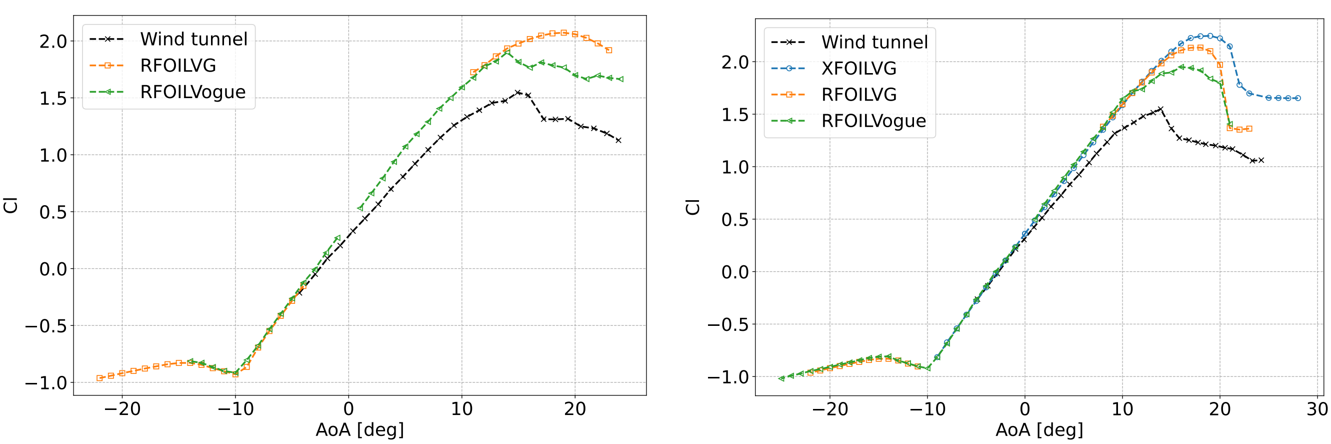

(a) 4 mm VGs placed at 20% chord, free transition

(b) 6 mm VGs placed at 30% chord, free transition

Figure 13. FFA-W3-241 airfoil with free transition and VGs placed on the upper side at 1.6 million Reynolds number. Wind tunnel data taken from Fuglsang et al. (1998).

300 RFOILVogue's predictions of stall margin variation with VG geometry parameters are also compared with the wind tunnel data. The vane size comparison between the larger 6 mm VGs and the smaller 4 mm VGs is shown in Figure 15. The comparison

https://doi.org/10.5194/wes-2025-69
Preprint. Discussion started: 6 May 2025

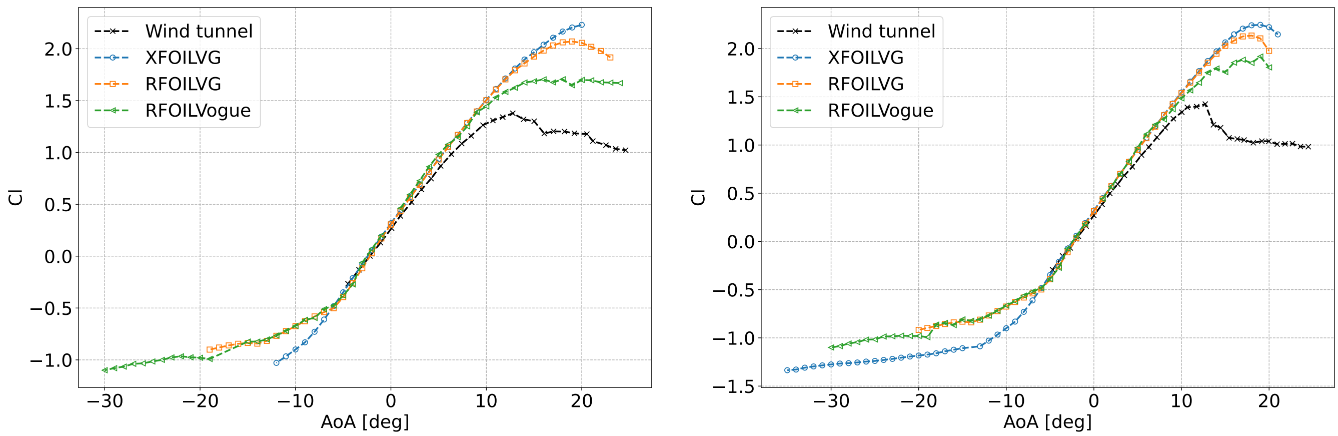

(a) 4 mm VGs placed at 20% chord, forced transition

(b) 6 mm VGs placed at 30% chord, forced transition

Figure 14. FFA-W3-241 airfoil with forced transition through zigzag tape and VGs placed on the upper side at 1.6 million Reynolds number Wind tunnel data taken from Fuglsang et al. (1998).

of VG locations is shown in Figure 16. Since drag data was unavailable for the experiments, the comparison between VG and no VG RFOIL drag values is included only to compare expected trends.

RFOILVogue correctly predicts that the 6 mm VGs are more effective at delaying stall than the 4 mm VGs in free transition conditions in Figure 15a. Larger VGs are also known from literature (Baldacchino et al., 2018) to produce more drag because they cause a larger obstruction to the incoming flow. This trend is also captured in the drag plot in Figure 15b.

RFOILVogue also correctly predicts in Figure 16a that placing VGs further upstream at 20% chord is more beneficial for stall delay than putting them at 30% chord for this airfoil at the tested Reynolds number under free transition conditions. Placing VGs further downstream is expected to reduce the drag (Baldacchino et al., 2018) because a smaller portion of the airfoil boundary layer experiences the VG mixing that increases skin friction. This trend is also observed in the drag plot in Figure 16b.

Thus, despite the over-prediction in maximum lift, the new model predicts the correct parametric trends for variation in VG geometry and placement, which shows the tool's utility for design optimisation studies.

6.2 Comparison for the DU-97-W-300 airfoil

The DU-97-W-300 airfoil was developed as a dedicated airfoil for wind turbine rotor blades (Timmer and van Rooij, 2003) and used in the AVATAR reference wind turbine (Schepers et al., 2015). It has a maximum thickness-to-chord ratio of 30%. The wind tunnel data for this airfoil (Baldacchino et al., 2018) was acquired in the TU Delft Low Turbulence Tunnel and is part of the tuning database for XFOILVG and RFOILVG. The model chord is $0.65\,m$, and the chord-wise Reynolds number is 2 million. The selected test case consists of both free transition and forced transition measurements, with transition forced through a zigzag tape of height $0.35\,mm$ at $x/c = 0.05$ on the upper side. The reported wind tunnel turbulence level corresponds

https://doi.org/10.5194/wes-2025-69
Preprint. Discussion started: 6 May 2025

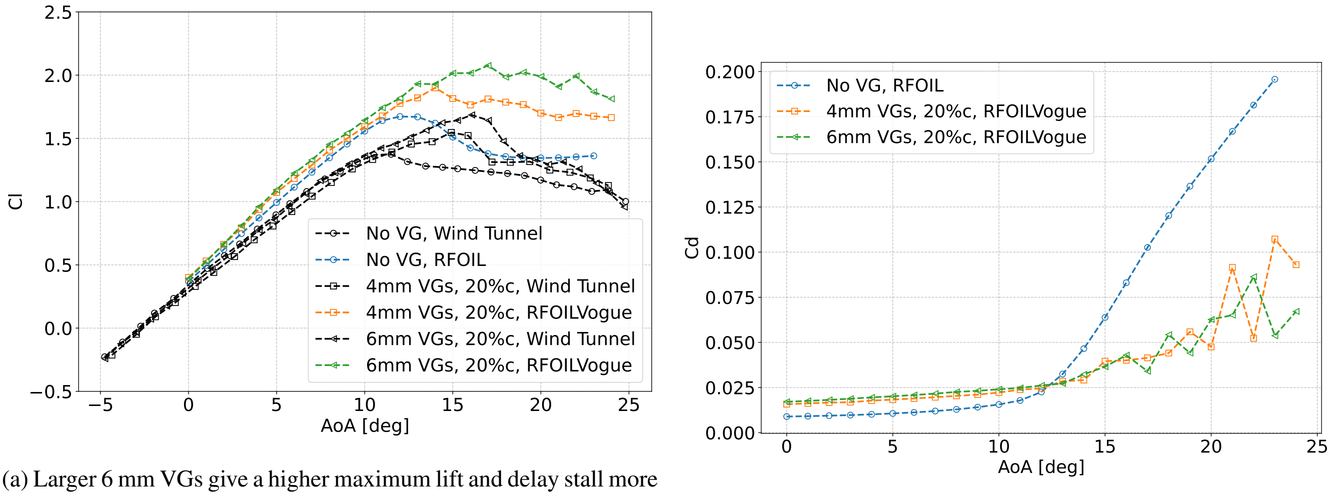

(a) Larger 6 mm VGs give a higher maximum lift and delay stall more than the smaller 4 mm VGs.

(b) Larger 6 mm VGs produce more drag than the smaller 4 mm VGs.

Figure 15. RFOILVogue predicts the expected maximum lift, stall delay, and drag trends when comparing VG sizes under free transition conditions. Wind tunnel data taken from Fuglsang et al. (1998).

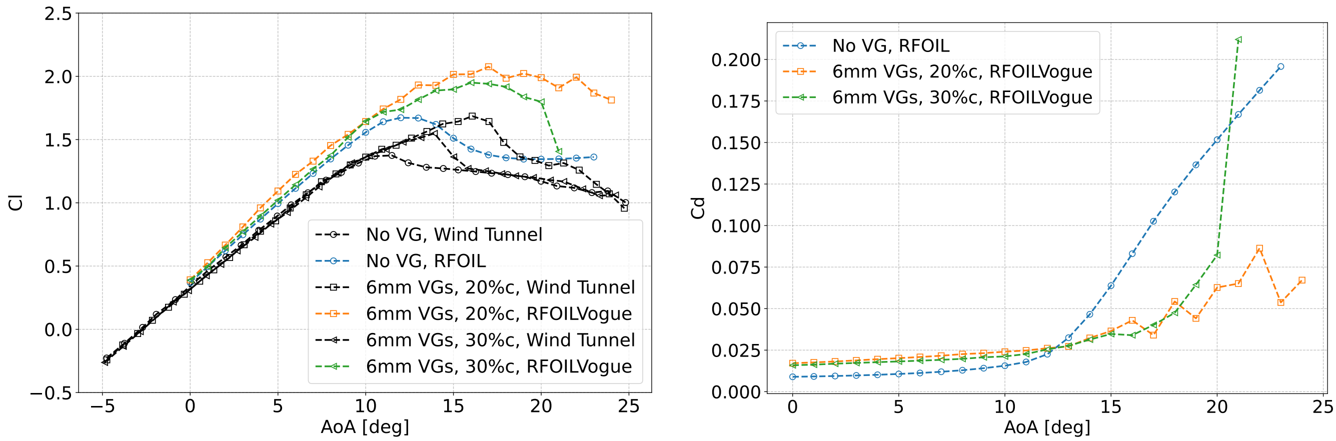

(a) Placing VGs further upstream at 20% chord delays stall by a higher margin than placing them at 30% chord.

(b) Placing VGs at 20% chord generates more drag than placing them at 30% chord.

Figure 16. RFOILVogue predicts the expected maximum lift, stall delay, and drag trends when comparing the chord-wise placement location of VGs under free transition conditions. Wind tunnel data taken from Fuglsang et al. (1998).

to $N = 9$ for the e^N transition check in the free transition calculations. Similar to the FFA-W3-241 case, the comparison for the no VG case in Figure 17 shows that RFOIL slightly over-predicts the lift slope polar and maximum lift. However, the free transition prediction is much closer to wind tunnel data for the DU-97-W-300 airfoil than the FFA-W3-241 airfoil.

https://doi.org/10.5194/wes-2025-69
Preprint. Discussion started: 6 May 2025

WIND ENERGY SCIENCE DISCUSSIONS

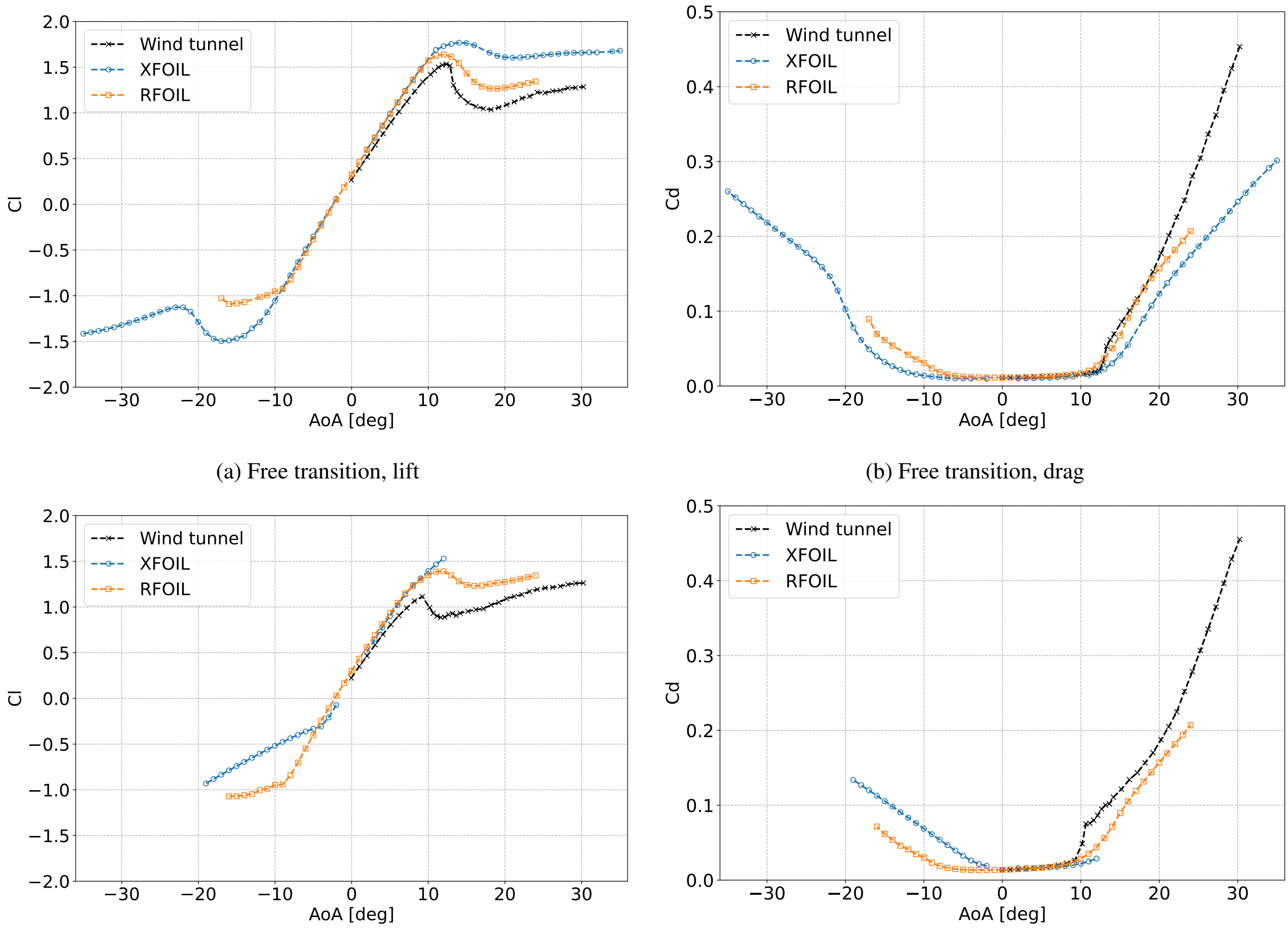

(a) Free transition, lift

(b) Free transition, drag

(c) Forced transition, lift

(d) Forced transition, drag

Figure 17. Establishing a baseline for RFOIL and XFOIL for the DU-97-W-300 airfoil at 2 million Reynolds number with and without forced transition by comparing the lift and drag characteristics. Wind tunnel data taken from Baldacchino et al. (2018).

The VG case selected for comparison in this section uses triangular vane VGs placed in a counterrotating array with the geometry parameters $h = 5mm$, $l = 15mm$, $D = 35mm$, $d = 17.5mm$, $\beta = 15°$, on the upper side. Compared to the experimental data, RFOILVogue performs at par with RFOILVG for the lift and drag in the linear region and the stall angle (Figure 18). RFOILVogue over-predicts the maximum lift and the post-stall drag compared to RFOILVG. Thus, the present analytical VG model that models the integral boundary layer quantities can predict the lift polar to a similar degree of accuracy as the former tuned engineering model that corrects the lift polar for VG effects.

The new model outperforms the older tuned models when predicting the actual boundary layer properties. The displacement and momentum thicknesses from the boundary layer are compared between RFOILVogue, RFOILVG, and fully-turbulent

https://doi.org/10.5194/wes-2025-69
Preprint. Discussion started: 6 May 2025

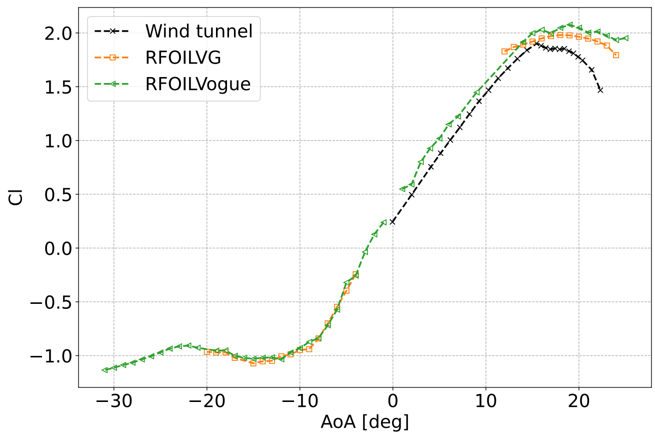

(a) Free transition, lift

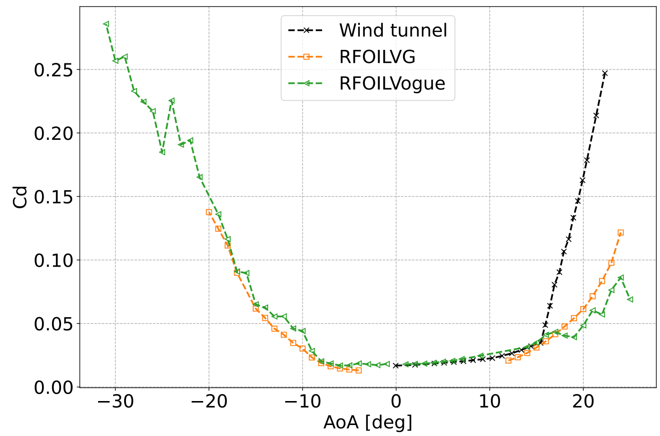

(b) Free transition, drag

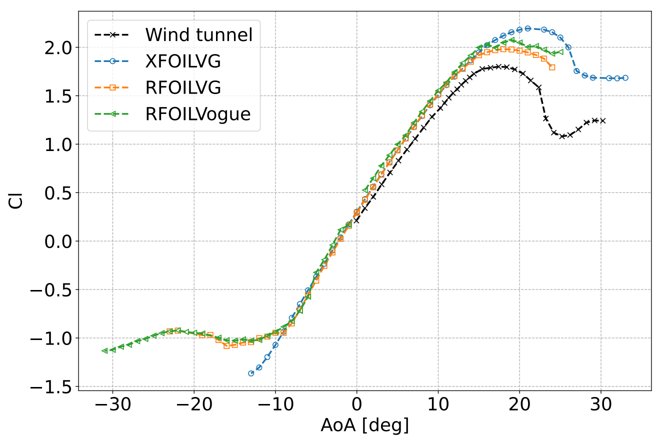

(c) Forced transition, lift

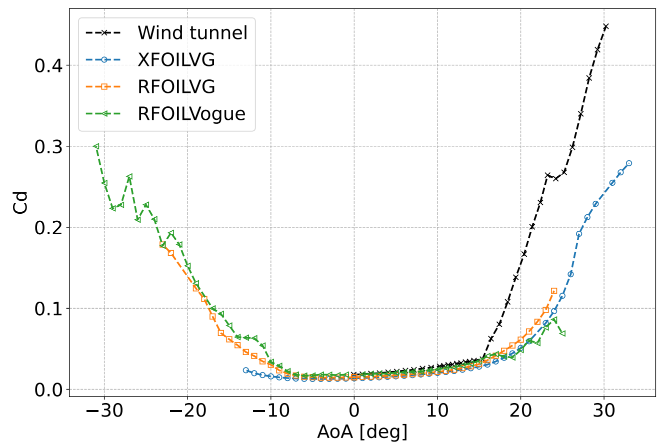

(d) Forced transition, drag

Figure 18. RFOILVogue predicts the same stall angle and slightly worse maximum lift than RFOILVG for the DU-97-W-300 airfoil with and without forced transition through zigzag tape with 5 mm VGs placed at 20% chord on the upper side at 2 million Reynolds number. Wind tunnel data taken from Baldacchino et al. (2018).

RANS CFD calculations of this airfoil and VGs in Figure 19. We select the case of 8° angle of attack where there is a strong pressure gradient, but the flow is still attached. This allows for comparing the model predictions for an adverse pressure gradient case to the zero pressure gradient flat plate.

The new RFOILVogue predicts a nearly identical value as CFD calculations for the displacement thickness at 8° angle of attack, except for a small part of the airfoil near the trailing edge. RFOILVG under-predicts the displacement thickness for the same case. RFOILVogue over-predicts the momentum thickness compared to CFD results, while RFOILVG under-predicts the momentum thickness. These results contrast the simulated flat plate case in Section 5. In the flat plate comparison, the VG model under-predicted the displacement thickness near the VG location and over-predicted the momentum thickness far from

https://doi.org/10.5194/wes-2025-69
Preprint. Discussion started: 6 May 2025

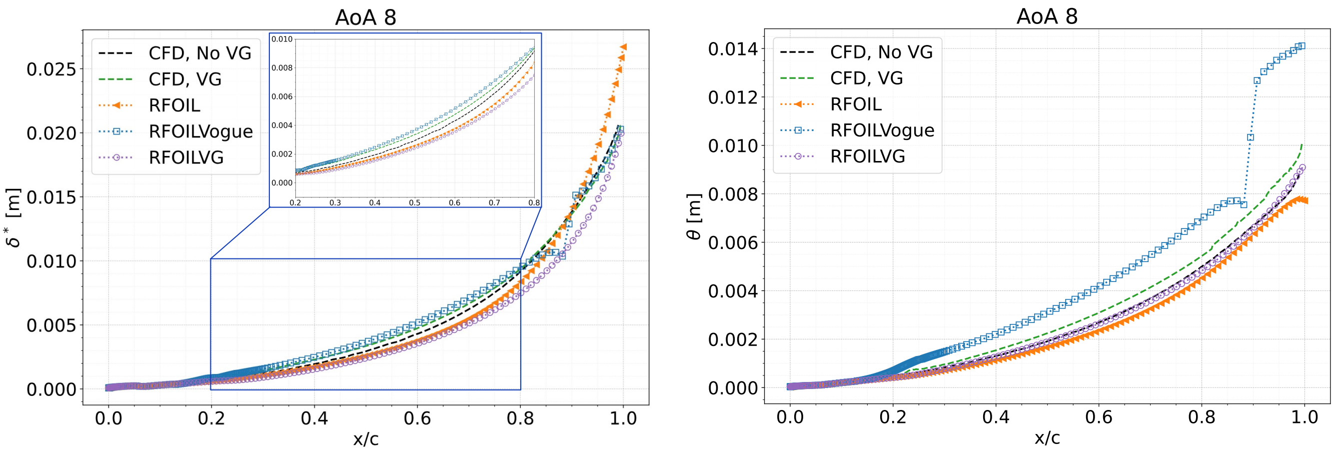

(a) Displacement thickness

(b) Momentum thickness

Figure 19. Comparing the displacement and momentum thicknesses predicted by RFOILVG and RFOILVogue for the DU-97-W-300 airfoil with forced transition through zigzag tape and 5mm VGs placed at 20% chord on the upper side at 8° angle of attack at 2 million Reynolds number

the VG location, resulting in a net lower shape factor and higher mixing. For the airfoil case, the VG model still predicts a higher mixing, but this time, mainly because of a higher momentum thickness estimation.

Thus, for the adverse pressure gradient airfoil case, the VG model predicts the mass transfer well but predicts a much higher momentum in the boundary layer than expected from CFD. This is attributed to the VG model being developed from zero pressure gradient flat plate flows and reaching its limitations when calculating adverse pressure gradient boundary layers. In adverse pressure gradient boundary layers, the momentum transfer is countered by the pressure gradient, which results in less momentum and energy in the boundary layer. The VG model does not account for this interaction and thus drives the boundary layer towards a higher momentum and energy than expected. Suggestions for future investigations to overcome this limitation due to model assumptions are discussed in Section 8.

7 Global Performance Assessment

Besides the selected cases discussed in Section 6, the performance of RFOILVogue and RFOILVG was compared for a broader database of airfoils equipped with VGs. The database consists both of cases used to tune RFOILVG and cases that fall outside of the training dataset. The accuracy and performance of RFOILVogue, RFOILVG, and XFOILVG in predicting the stall characteristics compared to wind tunnel data are summarised in Tables 2 and 3. A distinction is made between the code performance for the cases used to tune RFOILVG and those outside the training dataset. The code robustness is compared by comparing the number of converged angles of attack in a polar calculation between 0° and 35°, increasing in increments of 1°. The errors in stall characteristics are defined as in Equations (18) and (19). The standard deviation s of the errors for N

https://doi.org/10.5194/wes-2025-69
Preprint. Discussion started: 6 May 2025

test cases is defined as in Equation (20). The subscript '*WT*' refers to wind tunnel data, and '*code*' refers to the corresponding values from XFOIL or RFOIL as applicable.

$$\text{Error in stall angle, } \epsilon_\alpha = \alpha_{code} - \alpha_{WT} \tag{18}$$

$$\text{Error in maximum lift, } \epsilon_{C_l} = \frac{C_{l\,code} - C_{l\,WT}}{C_{l\,WT}} \tag{19}$$

$$s = \sqrt{\frac{1}{N-1}\sum_{i=1}^{N}(\epsilon_i - \overline{\epsilon})^2}, \quad \text{where } \overline{\epsilon} \text{ is the mean} \tag{20}$$

Table 2. Performance assessment of the VG models for cases outside the tuning dataset of XFOILVG and RFOILVG

	Number of Converged Angles (out of 36)			Error in Stall Angle [°]			Error in Maximum Lift [%]		
	XFOILVG	**RFOILVG**	**RFOILVogue**	**XFOILVG**	**RFOILVG**	**RFOILVogue**	**XFOILVG**	**RFOILVG**	**RFOILVogue**
Mean	20	17	18	7.5	3.4	1.2	50.3	36.3	23.6
Standard deviation	-	-	-	3.4	2.4	1.5	25.2	13.3	17.7

Table 3. Performance assessment of the VG models for the cases used to tune XFOILVG and RFOILVG

	Number of Converged Angles (out of 36)			Error in Stall Angle [°]			Error in Maximum Lift [%]		
	XFOILVG	**RFOILVG**	**RFOILVogue**	**XFOILVG**	**RFOILVG**	**RFOILVogue**	**XFOILVG**	**RFOILVG**	**RFOILVogue**
Mean	20	20	17	2.0	-0.1	1.6	17.9	10.0	6.9
Standard deviation	-	-	-	4.2	3.8	5.1	9.4	10.2	11.9

RFOILVogue overall improves over RFOILVG in the stall characteristics, predicting stall angles and maximum lift that are much closer to wind tunnel measurements. RFOILVogue captures the lift increase from the no VG to the VG case more accurately than RFOILVG. For some cases that are used to tune RFOILVG, RFOILVogue only improves over RFOILVG for the maximum lift predictions, while RFOILVG captures the stall angle better. In line with what is observed in earlier works for RFOIL and RFOILVG (Van Rooij, 1996; Sahoo et al., 2024), RFOILVogue also improves over XFOILVG overall. This, however, is attributed to the improvements of base RFOIL over base XFOIL rather than the improvements in the VG model.

Besides the improvements in accuracy, the new RFOILVogue is also more robust, providing a converged solution for more angles of attack than RFOILVG. This was particularly true for free transition cases, for instance the cases shown in Figures 13a,

https://doi.org/10.5194/wes-2025-69
Preprint. Discussion started: 6 May 2025

18a and 18b. This can be attributed to the new VG model's inclusion of the upstream effect of VGs on the boundary layer and its implementation of an earlier transition to turbulence upstream of the VG location, both missing in the VG model of RFOILVG. RFOILVG converges for more angles for the airfoils included in its training dataset.

The starting point of this upstream effect is fixed at 10 heights upstream of the VG location based on observations from flat plates (as described in Section 4.4). However, the boundary layer comparisons between CFD and RFOIL calculations for the DU97W300 airfoil in Figure 19 showed that the upstream effect starts closer to the VG location than 10 VG heights upstream. Capturing the upstream effect better can improve the robustness of the VG model even further. This is further elaborated in Section 8 in the reflection on the impact of the VG model's inherent assumptions derived from flat plate observations.

8 Conclusions and Future Work

In this work, we used observations from zero pressure gradient turbulent boundary layers under the effect of counter-rotating streamwise vortices to derive new spanwise-averaged Integral Boundary Layer equations valid for these boundary layers. We identified the changes in the shape factor and the additional viscous dissipation as the most significant. We proposed a model that connects the changes in the boundary layer to the vortex generator array geometry parameters and the flow Reynolds number. Using this model in RFOIL, we created an extended version named RFOILVogue that can analyse a broad range of airfoils and vortex generator configurations to calculate aerodynamic forces. A benchmark of RFOILVogue and the older RFOILVG against wind tunnel measurements of airfoils with VGs showed that RFOILVogue improves over its stall angle and maximum lift predictions.

While RFOILVogue is an improvement over RFOILVG, it still overestimates the maximum lift at stall by about 23% and the stall angle by about $1°$ on average. The reduction in lift post-stall is also under-predicted. Benchmarking the integral boundary layer quantities with CFD calculations reveals that the model inaccuracies become significant over severely adverse pressure gradient areas. Boundary layers with severely adverse pressure gradients deviate from the VG model's starting assumption of a zero pressure gradient flat plate. Refinement of the model for these severe pressure gradients will improve accuracy and robustness. Another area of improvement for the model is the refinement of the upstream effects of VGs for adverse pressure gradients. This will enhance accuracy in the free transition cases by predicting the impact of VGs on natural transition more accurately.

To incorporate the effects of strong pressure gradients in the IBL equations, the authors suggest investigating VG effects on turbulent boundary layers that deviate from equilibrium turbulent boundary layers. The turbulence shear lag equation encapsulates this deviation from equilibrium boundary layers. The impact of adverse pressure gradients is mainly contained in the $G-\beta$ relationship between the scaled pressure gradient and shape factor. Furthermore, the proposed model can be refined by applying the proposed methodology to thicker airfoils with more severe pressure gradients to refine further the relations between vortex generator parameters and boundary layer properties.

Overall, the new RFOILVogue is a more robust and generalised VG model than the earlier models, capable of modelling various families of airfoils and vortex generators. Besides the improvements in accuracy and robustness, the VG model derived

https://doi.org/10.5194/wes-2025-69
Preprint. Discussion started: 6 May 2025

from flat plate boundary layer observations also provides a methodology for improving VG models from flat plate boundary layer investigations without relying on expensive wind tunnel measurements of an extensive range of airfoils. The new VG model can be further enhanced by applying the model framework to more severely challenging flow conditions.

Author contributions. **Abhratej Sahoo:** Conceptualization, Methodology, Formal Analysis, Writing – Original Draft, **Akshay Koodly Ravishankara:** Conceptualization, Writing - Review & Editing, **Wei Yu:** Writing - Review & Editing, Supervision, **Daniele Ragni:** Writing - Review & Editing, Supervision, **Carlos Simao Ferreira:** Conceptualization, Supervision

Competing interests. The authors declare that no competing interests are present.

Acknowledgements. This work was carried out within the VoGUe project funded by a Privaat-Publieke Samenwerkingen-toeslag (PPS grant) awarded by the Netherlands Enterprise Agency (RVO). Partners involved in the VoGUe project are TNO, TU Delft, and Vestas Wind Systems A/S.

Appendix A: Deriving the Integral Boundary Layer equations for VGs

In incompressible form, the modified boundary layer equations for flat plates equipped with VGs are given in Equations (A1) to (A3). Compared to the no-VG methodology , the 2D approximation can no longer be applied to the VG boundary layer due to significant spanwise velocities and spanwise stresses, as highlighted in the respective equations. Additionally, unlike the no-VG case, the pressure inside the boundary layer is no longer invariant in the normal direction. The local increased velocity caused by the mixing due to the vortices creates local low-pressure regions inside the boundary layer. This local low pressure is significant in regions close to the VG location but recovers quickly as the vortices dissipate downstream of the VGs. Thus, the streamwise pressure gradient in the X momentum equation can no longer be reduced to a gradient of the streamwise velocity outside the boundary layer. To apply the IBL framework to VG boundary layers and maintain the original form of the IBL equations, the pressure inside the boundary layer p is split into an external component p_e and an induced component $p_{i,VG}$ due to the vortices (Equation (A4)). The external pressure varies only in the streamwise direction, while the induced pressure can vary in all directions influenced by the vortices.

Continuity Equation: $$\frac{\partial \overline{u}}{\partial x} + \frac{\partial \overline{v}}{\partial y} + \boxed{\frac{\partial \overline{w}}{\partial z}} = 0 \tag{A1}$$

X Momentum Equation: $$\overline{u}\frac{\partial \overline{u}}{\partial x} + \overline{v}\frac{\partial \overline{u}}{\partial y} + \boxed{\overline{w}\frac{\partial \overline{u}}{\partial z}} = -\frac{1}{\rho}\frac{\partial p}{\partial x} + \frac{1}{\rho}\left(\frac{\partial \tau_{yx}}{\partial y} + \boxed{\frac{\partial \tau_{zx}}{\partial z}}\right) \tag{A2}$$

https://doi.org/10.5194/wes-2025-69
Preprint. Discussion started: 6 May 2025

Open Access WIND ENERGY SCIENCE DISCUSSIONS

$$\text{Y Momentum Equation:} \quad \overline{u}\frac{\partial \overline{v}}{\partial x} + \overline{v}\frac{\partial \overline{v}}{\partial y} + \boxed{\overline{w}\frac{\partial \overline{v}}{\partial z}} = -\frac{1}{\rho}\frac{\partial p}{\partial y} + \frac{1}{\rho}\left(\frac{\partial \tau_{xy}}{\partial x} + \boxed{\frac{\partial \tau_{zy}}{\partial z}}\right) \tag{A3}$$

$$p = p_e + p_{i,VG} \tag{A4}$$

$$\frac{\partial p}{\partial x} = \frac{\partial p_e}{\partial x} + \frac{\partial p_{i,VG}}{\partial x} = -\rho U_e \frac{dU_e}{dx} + \frac{\partial p_{i,VG}}{\partial x} \tag{A5}$$

Thus, the continuity and X-momentum equations for VG boundary layers as expressed as shown in Equations (A6) and (A7) to derive the IBL equations.

$$\text{Continuity Equation:} \quad \frac{\partial \overline{u}}{\partial x} + \frac{\partial \overline{v}}{\partial y} + \boxed{\frac{\partial \overline{w}}{\partial z}} = 0 \tag{A6}$$

$$\text{X Momentum Equation:} \quad \overline{u}\frac{\partial \overline{u}}{\partial x} + \overline{v}\frac{\partial \overline{u}}{\partial y} + \boxed{\overline{w}\frac{\partial \overline{u}}{\partial z}} = U_e\frac{dU_e}{dx} - \boxed{\frac{1}{\rho}\frac{\partial p_{i,VG}}{\partial x}} + \frac{1}{\rho}\left(\frac{\partial \tau_{yx}}{\partial y} + \boxed{\frac{\partial \tau_{zx}}{\partial z}}\right) \tag{A7}$$

The IBL equations are calculated by taking the n$^{\text{th}}$ moment of the X-momentum equation and integrating along the boundary layer direction as shown in Equation (A8). $n = 0$ gives the IBL momentum equation and $n = 1$ gives the IBL kinetic energy equation.

$$(\text{X Momentum equation}) \cdot (n+1)u^n - (\text{Continuity Equation}) \cdot \left(U_e^{n+1} - u^{n+1}\right) \tag{A8}$$

To formulate an approximate 2D IBL system from the 3D form of the boundary layer equations, Equation (A8) is first integrated along the boundary layer height (y). Then, the equations are spanwise-averaged along the span (z). The spanwise flow is periodic along the span of a repeating VG pair unit. This gives

$$\frac{\int_{-D/2}^{D/2}\int_{0}^{\infty}\left((\text{X Momentum equation}) \cdot (n+1)u^n - (\text{Continuity Equation}) \cdot \left(U_e^{n+1} - u^{n+1}\right)\right) dydz}{\int_{-D/2}^{D/2} dz} \tag{A9}$$

Substituting $n = 0$ and $n = 1$ in Equation (A8) gives

$$\left(u\frac{\partial u}{\partial x} + v\frac{\partial u}{\partial y} + w\frac{\partial u}{\partial z}\right) - (U_e - u)\left(\frac{\partial u}{\partial x} + \frac{\partial v}{\partial y} + \frac{\partial w}{\partial z}\right) = U_e\frac{dU_e}{dx} - \frac{1}{\rho}\frac{\partial p_{i,VG}}{\partial x} + \frac{1}{\rho}\left(\frac{\partial \tau_{yx}}{\partial y} + \frac{\partial \tau_{zx}}{\partial z}\right) \tag{A10}$$

https://doi.org/10.5194/wes-2025-69
Preprint. Discussion started: 6 May 2025

eawe european academy of wind energy
Open Access WIND ENERGY SCIENCE DISCUSSIONS

$$2u\left(u\frac{\partial u}{\partial x}+v\frac{\partial u}{\partial y}+w\frac{\partial u}{\partial z}\right)-\left(U_e^2-u^2\right)\left(\frac{\partial u}{\partial x}+\frac{\partial v}{\partial y}+\frac{\partial w}{\partial z}\right)=2u\left(U_e\frac{\partial U_e}{\partial x}-\frac{1}{\rho}\frac{\partial p_{i,VG}}{\partial x}+\frac{1}{\rho}\left(\frac{\partial \tau_{yx}}{\partial y}+\frac{\partial \tau_{zx}}{\partial z}\right)\right) \tag{A11}$$

Equations (A10) and (A11) can be rearranged and integrated as shown in Equation (A9). The y-integral limits can be changed from $[0,\infty]$ to $[0,\delta]$ without affecting the integral equation because all the integrals are non-zero inside the boundary layer and zero outside. The Leibniz integral rule can be applied when integrating to obtain the spanwise-averaged formulation. The spanwise velocity w and the spanwise stress component τ_{zx} are zero on the spanwise bounding planes $z=\pm D/2$. An example of this from the CFD simulation is shown in Figure A1 for the case of the flat plate equipped with VGs of 5 mm height at a streamwise location of 10 heights downstream from the VG location at Reynolds number 2 million. This results in several integrals of the spanwise terms reducing to zero, as shown in Equations (A12) to (A15). Only the dissipative form of the spanwise shear stress gradient reduces to a non-zero value as shown in Equation (A16) and is later denoted as $C_{\mathcal{D}z}$.

$$\begin{aligned}\int_{-D/2}^{D/2}\int_0^{\delta}\frac{\partial}{\partial z}\left(w\left(U_e-u\right)\right)dydz &= \int_{-D/2}^{D/2}\frac{d}{dz}\left(\int_0^{\delta}\left(w\left(U_e-u\right)\right)dy\right)dz\\ &= \left(\int_0^{\delta}w\left(U_e-u\right)dy\right)\Bigg|_{z=D/2}-\left(\int_0^{\delta}w\left(U_e-u\right)dy\right)\Bigg|_{z=-D/2}=0\end{aligned} \tag{A12}$$

$$\int_{-D/2}^{D/2}\int_0^{\delta}-\frac{1}{\rho}\frac{\partial \tau_{zx}}{\partial z}dydz=\int_{-D/2}^{D/2}\frac{d}{dz}\left(\int_0^{\delta}-\frac{1}{\rho}\tau_{zx}dy\right)dz=\left(\int_0^{\delta}-\frac{1}{\rho}\tau_{zx}dy\right)\Bigg|_{z=D/2}-\left(\int_0^{\delta}-\frac{1}{\rho}\tau_{zx}dy\right)\Bigg|_{z=-D/2}=0 \tag{A13}$$

$$\begin{aligned}\int_{-D/2}^{D/2}\int_0^{\delta}\frac{\partial}{\partial z}\left(w\left(U_e^2-u^2\right)\right)dydz &= \int_{-D/2}^{D/2}\frac{d}{dz}\left(\int_0^{\delta}\left(w\left(U_e^2-u^2\right)\right)dy\right)dz\\ &= \left(\int_0^{\delta}w\left(U_e^2-u^2\right)dy\right)\Bigg|_{z=D/2}-\left(\int_0^{\delta}w\left(U_e^2-u^2\right)dy\right)\Bigg|_{z=-D/2}=0\end{aligned} \tag{A14}$$

$$\int_{-D/2}^{D/2}\int_0^{\delta}-\frac{1}{\rho}\frac{\partial}{\partial z}\left(u\tau_{zx}\right)dydz=\int_{-D/2}^{D/2}\frac{d}{dz}\left(\int_0^{\delta}-\frac{1}{\rho}u\tau_{zx}dy\right)dz=\left(\int_0^{\delta}-\frac{1}{\rho}u\tau_{zx}dy\right)\Bigg|_{z=D/2}-\left(\int_0^{\delta}-\frac{1}{\rho}u\tau_{zx}dy\right)\Bigg|_{z=-D/2}=0 \tag{A15}$$

https://doi.org/10.5194/wes-2025-69
Preprint. Discussion started: 6 May 2025

$$\int_{-D/2}^{D/2}\int_{0}^{\delta}\frac{2}{\rho}\tau_{zx}\frac{\partial u}{\partial z}dydz \equiv \int_{-D/2}^{D/2} C_{\mathcal{D}z}dz \neq 0 \tag{A16}$$

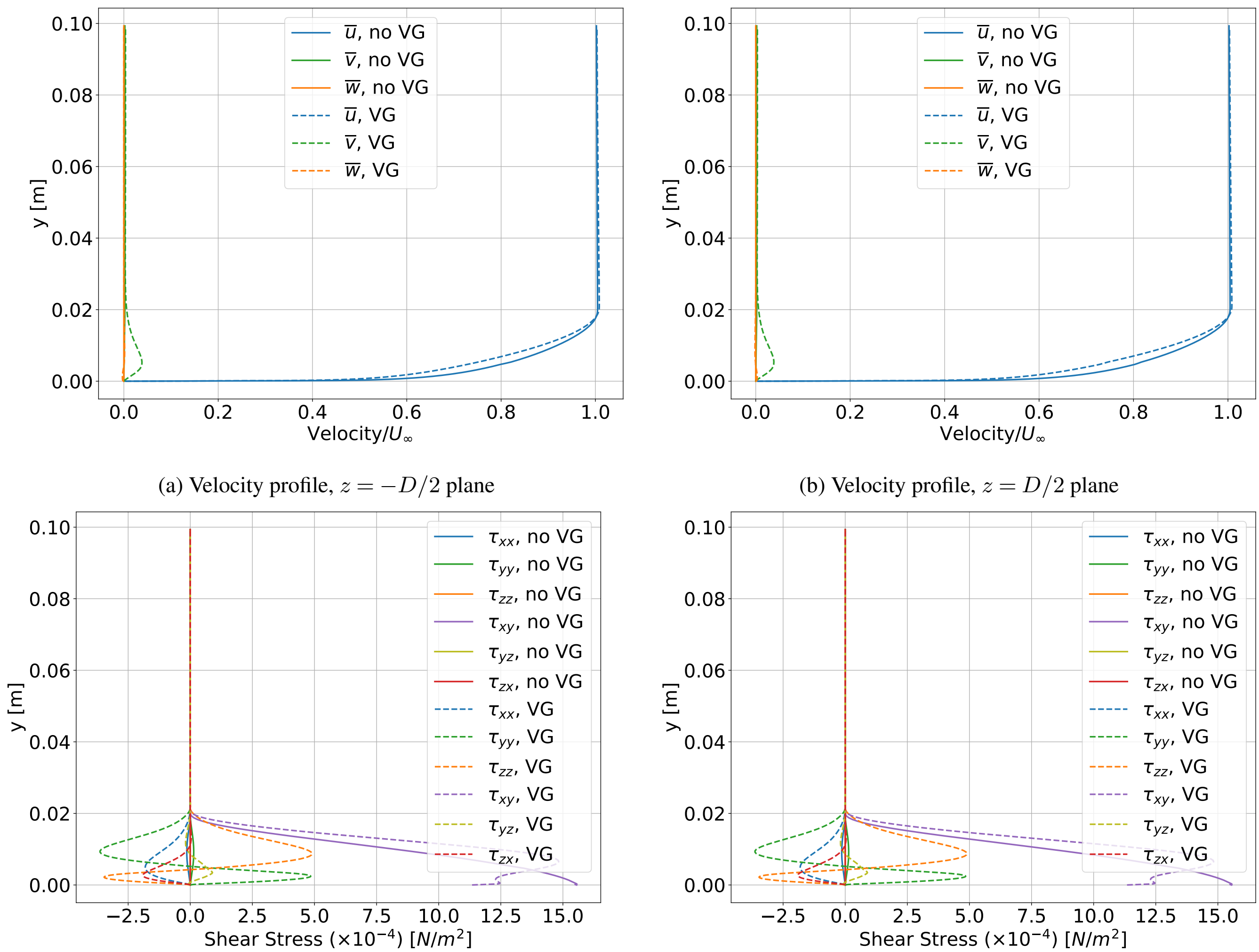

(a) Velocity profile, $z = -D/2$ plane

(b) Velocity profile, $z = D/2$ plane

(c) Shear Stress profile, $z = -D/2$ plane

(d) Shear Stress profile, $z = D/2$ plane

Figure A1. The spanwise velocity w and spanwise shear stress component τ_{zx} are zero at the spanwise bounding planes $z = \pm D/2$. This causes the integrals in Equations (A12) to (A15) to reduce to zero when deriving the IBL equations. The presented data is taken at a streamwise location 10 heights downstream of the VG location for the case described in Section 3.

This gives the IBL momentum equation (Equation (A17)) and the IBL kinetic energy equation (Equation (A18)). The new terms appearing due to VGs are highlighted. All pre-existing IBL quantities from the no-VG form have their usual meanings. A '—' over a quantity refers to its spanwise averaged form.

https://doi.org/10.5194/wes-2025-69
Preprint. Discussion started: 6 May 2025

eawe european academy of wind energy
Open Access WIND ENERGY SCIENCE DISCUSSIONS

$$\frac{d\overline{\theta}}{dx} = \frac{\overline{C_f}}{2} - \left(\overline{H}+2\right)\frac{\overline{\theta}}{U_e}\frac{dU_e}{dx} + \boxed{\overline{\left(\int_0^\infty \frac{\partial p_{i,VG}}{\partial x} dy\right)}} \tag{A17}$$

$$\frac{d\overline{H^*}}{dx} = 2\frac{\overline{C_\mathcal{D}}}{\overline{\theta}} - \frac{\overline{H^*}}{\overline{\theta}}\frac{\overline{C_f}}{2} + \left(\overline{H}-1\right)\frac{\overline{H^*}}{U_e}\frac{dU_e}{dx} + \boxed{\frac{2}{U_e^3\overline{\theta}}\overline{\left(\int_0^\delta \tau_{zx}\frac{\partial u}{\partial z}\right)}} + \boxed{\frac{2}{\rho U_e^3}\overline{\left(\int_0^\delta u\frac{\partial p_{i,VG}}{\partial x} dy\right)}} \tag{A18}$$

The IBL momentum equation for counterrotating VGs is identical to the equation for without VGs except for the local induced velocity/pressure contribution from the vortices. The increased momentum in the boundary layer is implicitly modelled in the increased shape factor and the increased skin friction coefficient. The IBL kinetic energy equation (Equation (A18)) has two additional terms – the term resulting from the local induced velocity contribution from the vortices and a dissipative term from the spanwise shear stress. This dissipative term can be interpreted as the additional kinetic energy added by the streamwise vortices due to the VGs to entrain higher-momentum flow from the upper parts of the boundary layer downward. Unlike the spanwise stresses themselves, the increase in kinetic energy due to the spanwise stresses does not cancel out over the span of one VG pair and is seen as a net dissipation term in the spanwise averaged equation. The term has a form similar to the already existing viscous dissipation term $C_\mathcal{D}$ from the no-VG boundary layers, as illustrated in Equation (A19). Thus, we denote the term as $C_{\mathcal{D}z}$ to denote that it arrives from the spanwise stresses.

$$C_\mathcal{D} = \frac{1}{\rho U_e^3}\int_0^\delta \left(\tau_{yx}\frac{\partial u}{\partial y}\right) dy, \quad C_{\mathcal{D}z} = \frac{1}{\rho U_e^3}\int_0^\delta \left(\tau_{zx}\frac{\partial u}{\partial z}\right) dy \tag{A19}$$

Hence, the final form of the IBL equations for incompressible turbulent span-averaged boundary layers due to counter-rotating VGs with a common downwash is

$$\frac{d\overline{\theta}}{dx} = \frac{\overline{C_f}}{2} - \left(\overline{H}+2\right)\frac{\overline{\theta}}{U_e}\frac{dU_e}{dx} + \boxed{\overline{\left(\int_0^\infty \frac{\partial p_{i,VG}}{\partial x} dy\right)}} \tag{A20}$$

$$\frac{d\overline{H^*}}{dx} = 2\frac{\overline{C_\mathcal{D}}}{\overline{\theta}} - \frac{\overline{H^*}}{\overline{\theta}}\frac{\overline{C_f}}{2} + \left(\overline{H}-1\right)\frac{\overline{H^*}}{U_e}\frac{dU_e}{dx} + \boxed{\frac{2\overline{C_{\mathcal{D}z}}}{\overline{\theta}}} + \boxed{\frac{2}{\rho U_e^3}\overline{\left(\int_0^\delta u\frac{\partial p_{i,VG}}{\partial x} dy\right)}} \tag{A21}$$

Appendix B: Verifying the validity of closures for turbulent flat plate boundary layers

The CFD simulations showed that the closures originally developed for turbulent flat plates without VGs still work well in predicting the IBL quantities in the case of VGs. The closures are additional relations accompanying the system of IBL equations to close the set of 3 equations containing 6 unknowns. The closures (Equations (B2) to (B4)) relate the kinetic energy shape factor H^*, the skin friction coefficient C_f, and the viscous dissipation coefficient $C_\mathcal{D}$ to the shape factor H and the momentum thickness Reynolds number Re_θ. Figure B1 shows how the closures compare between the VG and no VG cases.

$$\overline{H}_{CFD} = \left(\frac{\int_{-D/2}^{D/2} H dz}{\int_{-D/2}^{D/2} dz} \right)_{CFD} \tag{B1}$$

$$\overline{H^*}_{closure} = f\left(\overline{H}_{CFD}, \overline{Re_\theta}_{CFD}\right) \tag{B2}$$

$$\overline{C_f}_{closure} = f\left(\overline{H}_{CFD}, \overline{Re_\theta}_{CFD}\right) \tag{B3}$$

$$\overline{C_\mathcal{D}}_{closure} = f\left(\overline{C_f}_{closure}, \overline{H^*}_{closure}, \overline{C_\tau}_{CFD}, \overline{H}_{CFD}\right) \tag{B4}$$

Appendix C: Datasets for model benchmark

Table C1: Summary of reference data

Airfoil	**maximum thickness, t/c [%]**	**chord, c [m]**	**transition**	**chordwise Reynolds number [million]**	**VG location and geometry**	**Reference**
DU93W210	21	0.6	free	1	$x_{VG}/c = 0.2, 0.4, 0.6$ • $h = 5\,\mathrm{mm}, l = 17\,\mathrm{mm}, d = 10\,\mathrm{mm}, D = 35\,\mathrm{mm}, \beta = 16.4°$	Timmer and van Rooij (2003)

Continued on next page

https://doi.org/10.5194/wes-2025-69
Preprint. Discussion started: 6 May 2025

Table C1 – Continued from previous page

Airfoil	maximum thickness, t/c [%]	chord, c [m]	transition	chordwise Reynolds number [million]	VG location and geometry	Reference
DU91W2250	25	0.6	free	1	$x_{VG}/c = 0.2, 0.3$ • $h = 5\,\mathrm{mm}, l = 17\,\mathrm{mm}, d = 10\,\mathrm{mm}, D = 35\,\mathrm{mm}, \beta = 16.4°$	Timmer and van Rooij (2003)
DU97W300	30	0.65	• free • tripped at $0.05c$ upper side	2	$x_{VG}/c = 0.1, 0.2, 0.3, 0.4, 0.5$ • $h = 2.5\,\mathrm{mm}, l = 7.5\,\mathrm{mm}, d = 8.75\,\mathrm{mm}, D = 17.5\,\mathrm{mm}, \beta = 15°$ • $h = 5\,\mathrm{mm}, l = 15\,\mathrm{mm}, d = 17.5\,\mathrm{mm}, D = 35\,\mathrm{mm}, \beta = 15°$ • $h = 10\,\mathrm{mm}, l = 30\,\mathrm{mm}, d = 35\,\mathrm{mm}, D = 70\,\mathrm{mm}, \beta = 15°$	Baldacchino et al. (2018)
FFAW3241	24.1	0.6	• free • tripped at $0.05c$ upper side, $0.01c$ lower side	1.6	$x_{VG}/c = 0.1, 0.2, 0.3$ • $h = 4\,\mathrm{mm}, l = 12\,\mathrm{mm}, d = 20\,\mathrm{mm}, D = 28\,\mathrm{mm}, \beta = 19.5°$ • $h = 6\,\mathrm{mm}, l = 18\,\mathrm{mm}, d = 25\,\mathrm{mm}, D = 35\,\mathrm{mm}, \beta = 19.5°$	Fuglsang et al. (1998)
FFAW3301	30.1	—	free	3	$x_{VG}/c = 0.2, 0.3$ • $h/c = 0.01, l/c = 0.038, d/c = 0.06, D/c = 0.09, \beta = 15.5°$	Sørensen et al. (2014)

Continued on next page

https://doi.org/10.5194/wes-2025-69
Preprint. Discussion started: 6 May 2025

Table C1 – Continued from previous page

Airfoil	maximum thickness, t/c [%]	chord, c [m]	transition	chordwise Reynolds number [million]	VG location and geometry	Reference
FFAW3360	36	—	free	3	$x_{VG}/c = 0.15, 0.2$ • $h/c = 0.01, l/c = 0.038, d/c = 0.06, D/c = 0.09, \beta = 15.5°$	Sørensen et al. (2014)
FFAW3360	36	0.6	• free • tripped at $0.05c$ upper side, $0.01c$ lower side	3	$x_{VG}/c = 0.15, 0.2$ • $h = 6.75\,\mathrm{mm}, l = 12.4\,\mathrm{mm}, d = 15\,\mathrm{mm}, D = 54\,\mathrm{mm}, \beta = 15.5°$	received in private communication from Vestas

https://doi.org/10.5194/wes-2025-69
Preprint. Discussion started: 6 May 2025

eawe european academy of wind energy
Open Access WIND ENERGY SCIENCE DISCUSSIONS

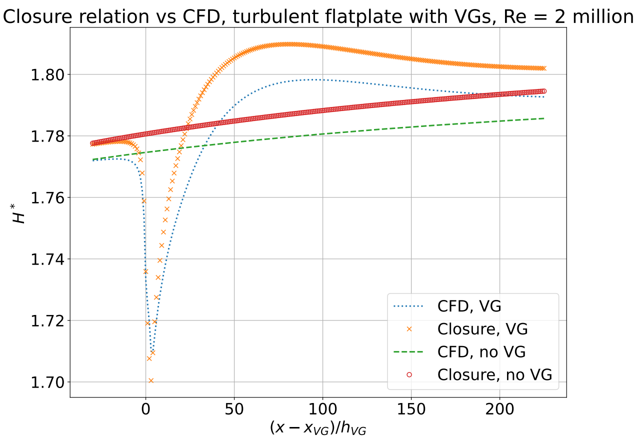

(a) Kinetic Energy Shape Factor

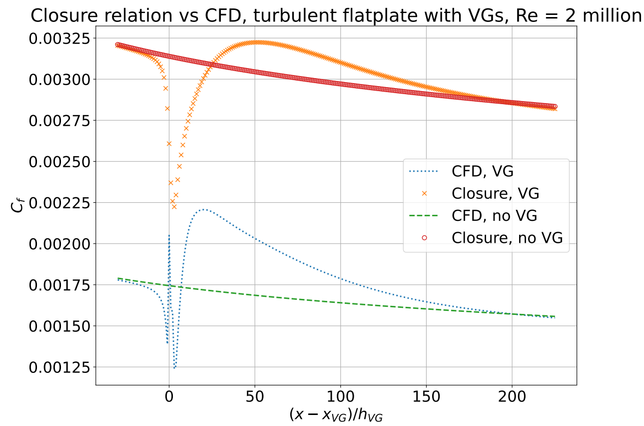

(b) Skin Friction Coefficient

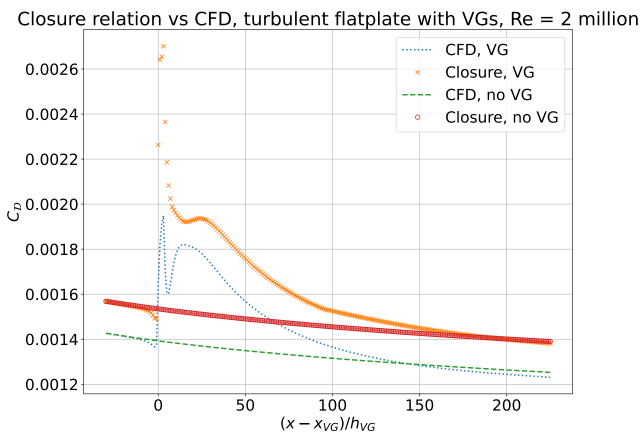

(c) Viscous Dissipation Coefficient

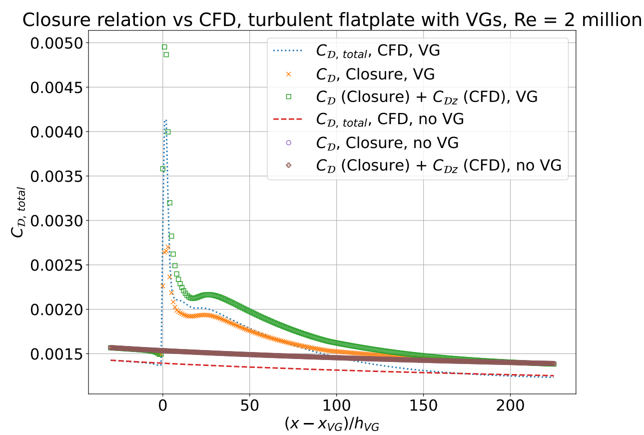

(d) Total Viscous Dissipation Coefficient

Figure B1. Comparing the closure relations to the CFD predictions for different IBL quantities at $Re_x = 2 \times 10^6$

References

Aparicio, M., Martín, R., Muñoz, A., and González, A.: Results of a parametric study of flow devices, guidelines for design, AVATAR project: WP3, 2015.

Bak, C., Skrzypiński, W., Gaunaa, M., Villanueva, H., Brønnum, N. F., and Kruse, E. K.: Full scale wind turbine test of vortex generators mounted on the entire blade, Journal of Physics: Conference Series, 753, 022 001, https://doi.org/10.1088/1742-6596/753/2/022001, 2016.

Baldacchino, D., Ragni, D., Simao Ferreira, C., and van Bussel, G.: Towards integral boundary layer modelling of vane-type vortex generators, in: 45th AIAA Fluid Dynamics Conference, p. 3345, American Institute of Aeronautics and Astronautics, Reston, Virginia, ISBN 978-1-62410-362-9, https://doi.org/10.2514/6.2015-3345, 2015.

Baldacchino, D., Ferreira, C., Tavernier, D. D., Timmer, W., and van Bussel, G. J. W.: Experimental parameter study for passive vortex generators on a 30% thick airfoil, Wind Energy, 21, 745–765, https://doi.org/10.1002/we.2191, 2018.

https://doi.org/10.5194/wes-2025-69
Preprint. Discussion started: 6 May 2025

Bardina, J., Huang, P., Coakley, T., Bardina, J., Huang, P., and Coakley, T.: Turbulence modeling validation, in: 28th Fluid Dynamics Conference, p. 2121, American Institute of Aeronautics and Astronautics, Reston, Virigina, https://doi.org/10.2514/6.1997-2121, 1997.

Bender, E. E., Anderson, B. H., and Yagle, P. J.: Vortex generator modeling for Navier-Stokes codes, in: 3rd ASME/JSME Joint Fluids Engineering Conference, p. 1, ISBN 0791819612, 1999.

Clauser, F. H.: Turbulent Boundary Layers in Adverse Pressure Gradients, Journal of the Aeronautical Sciences, 21, 91–108, https://doi.org/10.2514/8.2938, 1954.

Daniele, E., Schramm, M., Rautmann, C., Doosttalab, M., and Stoevesandt, B.: An extension of a strong viscous–inviscid coupling method for modeling the effects of vortex generators, Wind Engineering, 43, 175–189, 2019.

De Tavernier, D., Baldacchino, D., and Ferreira, C.: An integral boundary layer engineering model for vortex generators implemented in XFOIL, Wind Energy, 21, 906–921, 2018.

Drela, M.: XFOIL: An Analysis and Design System for Low Reynolds Number Airfoils, in: Low Reynolds Number Aerodynamics, edited by Mueller, T. J., 54), Berlin, Germany, Springer-Verlag, 1989, pp. 1–12, Springer Berlin Heidelberg, Berlin, Heidelberg, ISBN 0387518843, https://doi.org/10.1007/978-3-642-84010-4_1, 1989.

Drela, M., Giles, M., and Thompkins, W. T.: Newton Solution of Coupled Euler and Boundary-Layer Equations, in: Numerical and Physical Aspects of Aerodynamic Flows III, pp. 143–154, Springer New York, New York, NY, https://doi.org/10.1007/978-1-4612-4926-9_8, 1986.

Economon, T. D.: SU2 Tutorials - Incompressible Turbulent Flat Plate, https://su2code.github.io/tutorials/Inc_Turbulent_Flat_Plate/, 2018.

Economon, T. D.: Simulation and Adjoint-Based Design for Variable Density Incompressible Flows with Heat Transfer, AIAA Journal, 58, 757–769, https://doi.org/10.2514/1.J058222, 2020.

Economon, T. D., Palacios, F., Copeland, S. R., Lukaczyk, T. W., and Alonso, J. J.: SU2: An Open-Source Suite for Multiphysics Simulation and Design, AIAA Journal, 54, 828–846, https://doi.org/10.2514/1.J053813, 2016.

Fuglsang, P. L., Antoniou, I., Dahl, K., and Madsen, H. A.: Wind tunnel tests of the FFA-W3-241, FFA-W3-301 and NACA 63-430 airfoils, Riso-Reports-Riso R, 1041, 1–163, 1998.

Gonzalez, A., Baldacchino, D., Caboni, M. A. K., Kidambi, A., Manolesos, M., and Troldborg, N.: Aerodynamic flow control: Final report, Tech. rep., AVATAR Project, 2016.

Gonzalez-Salcedo, A., Croce, A., Arce Leon, C., Nayeri, C. N., Baldacchino, D., Vimalakanthan, K., and Barlas, T.: Blade Design with Passive Flow Control Technologies, in: Handbook of Wind Energy Aerodynamics, pp. 1–57, Springer International Publishing, Cham, https://doi.org/10.1007/978-3-030-05455-7_6-1, 2020.

Gould, D. G.: The use of vortex generators to delay boundary layer separation: theoretical discussion supported by tests on a CF-100 aircraft, Tech. rep., National Research Council of Canada. Division of Mechanical Engineering. National Aeronautical Establishment, https://doi.org/10.4224/23001523, 1956.

Green, J., Weeks, D., and Brooman, J.: Prediction of Turbulent Boundary Layers and Wakes in Compressible Flow by a Lag-Entrainment Method, Tech. Rep. 3791, Aeronautical Research Council London (England), 1977.

Gutiérrez, R., Llórente, E., Echeverría, F., and Ragni, D.: Wind tunnel tests for vortex generators mitigating leading-edge roughness on a 30% thick airfoil, Journal of Physics: Conference Series, 1618, 52 058, https://doi.org/10.1088/1742-6596/1618/5/052058, 2020.

Gutierrez-Amo, R., Fernandez-Gamiz, U., Errasti, I., and Zulueta, E.: Computational modelling of three different sub-boundary layer vortex generators on a flat plate, Energies, 11, 3107, https://doi.org/10.3390/en11113107, 2018.

Harris, C. D.: NASA Supercritical Airfoils. A Matrix of Family-Related Airfoils, Tech. rep., NASA Langley Research Centre, 1990.

Jensen, P. H., Chaviaropolos, T., and Natarajan, A.: LCOE reduction for the next generation offshore wind turbines: Outcomes from the INNWIND.EU project, Innwind.eu, 325, 2017.

Jirásek, A.: Vortex-generator model and its application to flow control, Journal of Aircraft, 42, 1486–1491, https://doi.org/10.2514/1.12220, 2005.

Kerho, M. F. and Kramer, B. R.: Enhanced airfoil design incorporating boundary layer mixing devices, in: 41st Aerospace Sciences Meeting and Exhibit, p. 211, ISBN 9781624100994, https://doi.org/10.2514/6.2003-211, 2003.

Lin, J. C.: Review of research on low-profile vortex generators to control boundary-layer separation, Progress in Aerospace Sciences, 38, 389–420, https://doi.org/10.1016/S0376-0421(02)00010-6, 2002.

Lögdberg, O., Fransson, J. H. M., and Alfredsson, P. H.: Streamwise evolution of longitudinal vortices in a turbulent boundary layer, Journal of Fluid Mechanics, 623, 27, 2009.

Manolesos, M., Papadakis, G., and Voutsinas, S. G.: Revisiting the assumptions and implementation details of the BAY model for vortex generator flows, Renewable Energy, 146, 1249–1261, https://doi.org/10.1016/j.renene.2019.07.063, 2020.

McKenna, R., Ostman, P., and Fichtner, W.: Key challenges and prospects for large wind turbines, Renewable and Sustainable Energy Reviews, 53, 1212–1221, https://doi.org/10.1016/j.rser.2015.09.080, 2016.

Özdemir, H.: Interacting Boundary Layer Methods and Applications, Handbook of Wind Energy Aerodynamics, pp. 1–53, 2020.

Ramanujam, G., Özdemir, H., and Hoeijmakers, H. W. M.: Improving airfoil drag prediction, Journal of aircraft, 53, 1844–1852, 2016.

Ravishankara, A. K., Bakhmet, I., and Özdemir, H.: Estimation of roughness effects on wind turbine blades with vortex generators, Journal of Physics: Conference Series, 1618, 52 031, https://doi.org/10.1088/1742-6596/1618/5/052031, 2020.

Rumsey, C., Smith, B., and Huang, G.: Description of a Website Resource for Turbulence Modeling Verification and Validation, in: 40th Fluid Dynamics Conference and Exhibit, p. 4742, American Institute of Aeronautics and Astronautics, Reston, Virigina, ISBN 978-1-60086-956-3, https://doi.org/10.2514/6.2010-4742, 2010.

Sahoo, A., Ferreira, C. S., Ravishankara, A. K., Schepers, G., and Yu, W.: Validation of an engineering model for vortex generators in a viscous-inviscid interaction method for airfoil analysis, Journal of Physics: Conference Series, 2647, 112 012, https://doi.org/10.1088/1742-6596/2647/11/112012, 2024.

Schepers, J. G., Ceyhan, O., Savenije, F. J., Stettner, M., Kooijman, H. J., Chaviarapoulos, P., Sieros, G., Simao Ferreira, C. S., Sørensen, N., Wächter, M., Stoevesandt, B., Lutz, T., Gonzalez, A., Barakos, G., Voutsinas, A., Croce, A., and Madsen, J.: AVATAR: Advanced aerodynamic tools for large rotors, in: 33rd Wind Energy Symposium, pp. 291–310, American Institute of Aeronautics and Astronautics Inc.(AIAA), https://doi.org/10.2514/6.2015-0497, 2015.

Schubauer, G. B. and Spangenberg, W. G.: Forced mixing in boundary layers, Journal of Fluid Mechanics, 8, 10, https://doi.org/10.1017/S0022112060000372, 1960.

Snel, H., Houwink, R., and Bosschers, J.: Sectional prediction of 3-D effects for stalled flow on rotating blades and comparison with measurements, Netherlands Energy Research Foundation ECN, 93, 395–399, 1993.

Snel, H., Houwink, R., and Bosschers, J.: Sectional prediction of lift coefficients on rotating wind turbine blades in stall, Ecn-C–93-052, 1994.

Sørensen, N. N., Zahle, F., Bak, C., and Vronsky, T.: Prediction of the Effect of Vortex Generators on Airfoil Performance, Journal of Physics: Conference Series, 524, 012 019, https://doi.org/10.1088/1742-6596/524/1/012019, 2014.

https://doi.org/10.5194/wes-2025-69
Preprint. Discussion started: 6 May 2025

Spalart, P. and Allmaras, S.: A one-equation turbulence model for aerodynamic flows, in: 30th Aerospace Sciences Meeting and Exhibit, 1, pp. 5–21, American Institute of Aeronautics and Astronautics, Reston, Virigina, ISSN 00341223, https://doi.org/10.2514/6.1992-439, 1992.

Spalart, P. R. and Garbaruk, A. V.: Correction to the Spalart–Allmaras Turbulence Model, Providing More Accurate Skin Friction, AIAA Journal, 58, 1903–1905, https://doi.org/10.2514/1.J059489, 2020.

Squire, H. B.: The Growth of a Vortex in Turbulent Flow, Aeronautical Quarterly, 16, 302–306, https://doi.org/10.1017/s0001925900003516, 1965.

Swafford, T. W.: Analytical approximation of two-dimensional separated turbulent boundary-layer velocity profiles, AIAA journal, 21, 923–926, 1983.

Timmer, W. A. and van Rooij, R. P. J. O. M.: Summary of the Delft University Wind Turbine Dedicated Airfoils, Journal of Solar Energy Engineering, 125, 488–496, https://doi.org/10.1115/1.1626129, 2003.

Van Ingen, J. L.: The eN method for transition prediction. Historical review of work at TU Delft, 38th AIAA Fluid Dynamics Conference and Exhibit, https://doi.org/10.2514/6.2008-3830, 2008.

Van Rooij, R.: Modification of the boundary layer calculation in RFOIL for improved airfoil stall prediction, 1996.

Velte, C. M., Braud, C., Coudert, S., and Foucaut, J.-M.: Vortex Generator Induced Flow in a High Re Boundary Layer, Journal of Physics: Conference Series, 555, 012 102, https://doi.org/10.1088/1742-6596/555/1/012102, 2014.

Von Stillfried, F., Lögdberg, O., Wallin, S., and Johansson, A. V.: Statistical modeling of the influence of turbulent flow separation control devices, 47th AIAA Aerospace Sciences Meeting including the New Horizons Forum and Aerospace Exposition, https://doi.org/10.2514/6.2009-1501, 2009.

von Stillfried, F., Wallin, S., and Johansson, A. V.: Evaluation of a Vortex Generator Model in Adverse Pressure Gradient Boundary Layers, AIAA Journal, 49, 982–993, https://doi.org/10.2514/1.J050680, 2011.

White, F. M.: Viscous fluid flow, McGraw-Hill Higher Education, ISBN 9780071244930, 2006.

Whitfield, D. L.: Integral Solution of Compressible Turbulent Boundary Layers Using Improved Velocity Profiles, Tech. rep., Arnold Engineering Development Center, 1978.

Yu, W., Bajarūnas, L. K., Zanon, A., and Ferreira, C. J. S.: Modeling dynamic stall of an airfoil with vortex generators using a double-wake panel model with viscous–inviscid interaction, Wind Energy, 27, 277–297, https://doi.org/10.1002/we.2889, 2024.

Zahle, F., Barlas, T., Lønbæk, K., Bortolotti, P., Zalkind, D., Wang, L., Labuschagne, C., Sethuraman, L., and Barter, G.: Definition of the IEA Wind 22-Megawatt Offshore Reference Wind Turbine, Tech. rep., ISBN 978-87-87335-71-3, https://doi.org/10.11581/DTU.00000317, 2024.